Allosteric modulation of the CXCR4:CXCL12 axis by targeting receptor nanoclustering via the TMV-TMVI domain

Eva M. García-Cuesta[1], Pablo Martínez[1], Karthik Selvaraju[2], Adrián Miguel Gómez Pozo[3], Gianluca D'Agostino[1], Sofía Gardeta[1], Adriana Quijada-Freire[1], Patricia Blanco Gabella[3], Carlos Roca[3], Rodrigo Jiménez-Saiz[1,4-6], Alfonso García-Rubia[3], Blanca Soler-Palacios[1], Pilar Lucas[1], Rosa Ayala-Bueno[1], Noelia Santander Acerete[1], Yolanda R. Carrasco[7], Ana Martínez[3,8], Nuria E Campillo[3,9], Lasse Jenssen[2], José Miguel Rodríguez-Frade[1], César Santiago[10], Mario Mellado[1*].

[1] Chemokine Signaling group, Department of Immunology and Oncology, Centro Nacional de Biotecnología/CSIC, Campus de Cantoblanco, 28049, Madrid, Spain.
[2] Division of Diagnostics and Specialist Medicine, Department of Health, Medical and Caring Sciences, Linköping University, 58185, Linköping, Sweden.
[3] Centro de Investigaciones Biológicas Margarita Salas (CIB-CSIC), 28040, Madrid, Spain.
[4] Department of Immunology, Instituto de Investigación Sanitaria Hospital Universitario de La Princesa (IIS-Princesa), 28006, Madrid, Spain.
[5] Department of Medicine, McMaster Immunology Research Centre (MIRC), Schroeder Allergy and Immunology Research Institute, McMaster University, Hamilton, ON L8S 4L8, Canada.
[6] Faculty of Experimental Sciences, Universidad Francisco de Vitoria (UFV), 28223, Madrid, Spain.
[7] B Lymphocyte Dynamics, Department of Immunology and Oncology, Centro Nacional de Biotecnología (CNB)/CSIC, Campus de Cantoblanco, 28049, Madrid, Spain.
[8] Neurodegenerative Diseases Biomedical Research Network Center (CIBERNED), Instituto de Salud Carlos III, 28029 Madrid, Spain
[9] Institute of Mathematical Sciences (ICMAT/CSIC), Campus de Cantoblanco, UAM, 28049 Madrid, Spain.
[10] X-ray Crystallography Unit, Department of Macromolecules Structure, Centro Nacional de Biotecnología/CSIC, Campus de Cantoblanco, 28049, Madrid, Spain.

[*]Corresponding author: Mario Mellado, Department of Immunology and Oncology, CNB/CSIC, Darwin 3, Cantoblanco, 28049 Madrid Spain. Tel: (+34) 91/585-4852; Fax: (+34) 91/372-0493; **Email:** mmellado@cnb.csic.es

Author Contributions: J.M.R.-F., C.S. and M.M. conceptualized the project and designed all aspects of the study; A.M.G.P. carried out the virtual computational screening; P.B.G. and C.R. performed docking analysis and evaluated the molecular dynamics, A.G.-R. synthesized the organic compounds. N.E.C. and A.M. contributed the analysis of the *in silico* results; E.M.G.-C., J.M.R.-F., P.M., G.D'A., S.G., A.Q-F., R.J.-S., B.S.-P., P.L., R.A.-B. and N.S.A. performed experiments; E.M.G.-C. and J.M.R.-F. quantified the TIRFM images; C.S. modeled the crystal packing structure and determined the mutations on CXCR4; P.M., S.G., and Y.R.C. performed the experiments on lipid bilayers; K.S: and L.J. developed the ZTX model; L.J. designed the ZTX model for the *in vivo* analysis; R.J.-S., Y.R.C., N.E.C., J.M.R.-F., C.S., and M.M. provided input into the project; J.M.R.-F., C.S., and M.M. wrote the manuscript.

Competing Interest Statement: E.M.G.-C., J.M.R.-F., N.E.C., A.M., C.S., and M.M. have a patent for compounds AGR1.131, AGR1.135 and AGR1.137. The remaining authors declare no potential conflict of interest.

Classification: Biological Science, Immunology and inflammation.

Keywords: cell migration, chemokine receptors, allosteric inhibitors

Abstract

CXCR4 is a ubiquitously expressed chemokine receptor that regulates leukocyte trafficking and arrest in homeostatic and pathological states, and also participates in organogenesis, HIV-1 infection and tumor development. Despite the potential therapeutic benefit of CXCR4 antagonists, so far only one, plerixafor (AMD3100), which blocks the ligand-binding site, has reached the clinic. Recent advances in imaging and biophysical techniques have provided a richer understanding of the membrane organization and dynamics of this receptor. CXCL12 activation of CXCR4 reduces the number of CXCR4 monomers/dimers at the cell membrane and increases the formation of large nanoclusters, which are largely immobile and are required for correct cell orientation towards chemoattractant gradients. Mechanistically, CXCR4 activation involves a structural motif defined by residues on TMV and TMVI of CXCR4. Using this structural motif as a template, we performed *in silico* molecular modeling followed by *in vitro* screening of a small compound library to search for allosteric antagonists of CXCR4 that do not affect CXCL12 binding. We identified AGR1.137, a small compound that abolishes CXCL12-mediated receptor nanoclustering and dynamics and blocks the ability of cells to sense CXCL12 gradients both *in vitro* and *in vivo* without altering ligand binding or receptor internalization.

Significance Statement

CXCR4 is a ubiquitous chemokine receptor that regulates leukocyte trafficking and arrest in homeostatic and pathological states. Yet, the only commercial CXCR4 antagonist approved for clinical use is plerixafor (AMD3100), a small compound that blocks the ligand-binding site. Unfortunately, its clinical application is limited by poor pharmacokinetics and adverse effects associated with long-term administration. Here, we performed *in silico* analyses of a small aromatic compound library followed by *in vitro* screening to identify allosteric CXCR4 antagonists that abrogate the ability of cells to sense chemoattractant gradients without altering other ligand-mediated functions such as blockade of cAMP production or receptor internalization. The selected compounds also acted *in vivo,* as demonstrated by reduced tumorigenesis and metastasis in a zebrafish tumor model. Our study describes a new approach to selectively alter some GPCR functions without the need for abolishing all receptor functionality.

Introduction

CXC chemokine receptor 4 (CXCR4) is a homeostatic G protein-coupled receptor (GPCR) that is widely expressed both in embryonic and adult tissues (1). It is also ubiquitously expressed in the hematopoietic system, where it plays important roles in leukocyte trafficking and arrest in specific niches both under homeostasis and disease. CXCR4 is essential for adaptive and innate immune responses as well as for bone marrow (BM) organization and maintenance (2). Indeed, CXCR4 and its unique chemokine ligand, CXCL12, are largely responsible for hematopoietic stem cell migration (3), homing (4) and survival (5) in the BM.

Results from studies in conditional *Cxcr4*-knockout mice point to a relevant role for CXCR4 in several non-hematopoietic tissues, for example, in regulating central nervous system development (6), and in vasculature development in the gastrointestinal tract (7) and the kidney (8). In addition, CXCR4, together with CCR5, serve as primary co-receptors (with CD4) for HIV-1 fusion and entry into target cells (9).

CXCR4 expression is frequently elevated in many cancers, including breast (10), ovarian (11), prostate (12), melanoma (13) and neuroblastoma (14), where it participates in tumor growth, tumor cell interactions with the microenvironment (15), vasculogenesis, angiogenesis (16) and metastasis (10). Indeed, increased CXCR4 expression in metastatic lesions correlates with tumor progression and with preferential metastatic sites of the primary tumor (17). Murine studies have suggested that CXCR4 is a good target in cancer therapy since blockade of its signaling impairs metastasis in different models (10, 18). Despite the essential role of the CXCR4/CXCL12 axis in physiology and pathology, the only commercial CXCR4 antagonist approved for clinical use is

plerixafor (AMD3100), which is indicated for mobilizing stem cells from the BM to the peripheral blood in autologous transplantation (19).

Using Single-Particle Tracking in Total Internal Reflection Fluorescence mode (SPT-TIRF) and STimulated Emission Depletion super resolution microscopy (STED), it has been demonstrated that CXCR4 is organized at the cell membrane as monomers, dimers and small aggregates (groups of ≥3 receptors) termed nanoclusters, and that CXCL12 binding reduces the percentage of monomers/dimers, and increases the formation of large nanoclusters (20). This is an essential mechanism to drive CXCR4 signaling that allows correct cell orientation towards CXCL12 gradients (21). A triple-mutant CXCR4 (K239L/V242A/L246A; CXCR4mut) dimerizes but neither forms nanoclusters in response to CXCL12 nor supports CXCL12-induced directed cell migration, although it can still trigger some Ca^{2+} flux and is internalized after ligand binding (20). In CXCR4, it has been identified a cluster defined by TMV and TMVI residues that conform a hydrophobic lock interconnecting the signal coming from the orthosteric ligand-binding site with the downstream conserved domains involved in G protein coupling and signaling (22, 23).

Here, we used this signal propagation domain of CXCR4 as the starting point to search for new CXCR4 antagonists. We performed *in silico* screening of a small aromatic compound library to identify potential allosteric antagonists that block directed cell migration, without affecting ligand binding and, therefore, allowing other CXCL12-mediated functions. Applying molecular modeling analyses, we identified a novel class of structurally-related low molecular weight compounds that modulate some CXCR4 functions by binding to a new regulatory cleft formed by the TMV and TMVI transmembrane helices. One of the selected compounds, AGR1.137, abrogated CXCL12-mediated receptor nanoclustering and dynamics and, consequently, the ability of the cells to specifically sense CXCL12 gradients, but did not alter ligand binding or receptor internalization. Notably, AGR1.137 had little effect on ERK1/2 and AKT phosphorylation, which may minimize the side effects associated with full CXCR4 inhibition. Finally, using a zebrafish model, we observed that AGR1.137 treatment of HeLa cells reduced tumorigenesis and metastasis, indicating that AGR1.137 also impairs cell sensitivity towards CXCL12 gradients by disassembling CXCR4 nanoclustering *in vivo*. In sum, our results establish the importance of residues in the TMV–VI cavity for CXCR4 nanoclustering and CXCL12-mediated directional migration, and identify a partial antagonist that operates both *in vitro* and *in vivo*.

Results

Screening for small compounds targeting CXCR4 that block CXCL12-induced CXCR4 nanoclustering

In CXCR4, the propagation domain that connects the ligand binding with the residues implicated in G-protein association, involves residues present in the area limited by transmembrane helices TMV and TMVI, which enclose a cleft of around 900 $Å^2$ (22) that is surface-exposed for interactions with the plasma membrane, and includes the residues implicated in receptor activation and in transmission of conformational changes through the TM helix domains (22) (Fig. 1A). We thus screened for allosteric antagonists matching this CXCR4 cleft and fitting into the cavity formed by TMV and TMVI but not impacting the CXCL12 binding site. Virtual screenings were performed using the MBC library (CIB-CSIC) (24) that contains more than 2,000 small heterocyclic compounds with drug-like properties. The compounds were prepared and docked using "Glide" against the modeled CXCR4 structure prepared using the SwissModel server (25). The compounds identified were then ranked by docking-score given by Glide and visualization of the poses.

In total, 40 candidates showed minimal interaction energy in the area of interest and were selected for functional analysis (Supplementary Table 1). We first screened their ability to block CXCL12-induced cell dependent migration in Transwell chambers.

Jurkat cells that were either untreated or treated with 50 μM of the selected small compounds (30 minutes, 37°C, 5% CO_2) were allowed to migrate towards CXCL12 (12.5 nM, 120 minutes, 37ºC, 5% CO_2). To enhance the possible inhibitory effects, the compounds were

maintained in the upper chamber containing the cells throughout the chemotaxis experiment (Supplementary Fig. 1A,B).

Based on these results, we initially selected two compounds, AGR1.135 and AGR1.137, which showed reproducible dose-dependent inhibitory effects on CXCR4-induced cell migration (Fig. 1B). As a control for further analysis, we used AGR1.131, which is also theoretically directed against the same motif on CXCR4 as AGR1.135 and AGR1.137 and shows minimal interaction energy, but fails to impact CXCL12-promoted cell migration. Under these experimental conditions, none of the selected compounds were toxic against Jurkat cells, as shown by propidium iodide incorporation and cell cycle analysis (Supplementary Fig. 1C). Structurally, the three selected compounds were verified using NMR (Supplementary information), and were characterized by the presence of a common core (4-(1-benzyl-1H-1,2,3-triazol-4-yl)phenyl) methanol, connected through a benzamide with a lateral chain bearing amines of different length and chemical nature. AGR1.131 bears a simple benzylamine, AGR1.135 contains a complex lateral chain due to the presence of the 1-(2-nitro-4-(trifluoromethyl)phenyl)piperazine, and AGR1.137 incorporates ethyl piperidine-4-carboxylate (Fig. 1C).

AGR1.135 and AGR1.137 block CXCL12-mediated CXCR4 nanoclustering and dynamics

The initial virtual screening was made based on interactions between low molecular weight compounds and the TMV–TMVI region on CXCR4. We next evaluated whether the selected compounds altered CXCL12-mediated CXCR4 nanoclustering and dynamics. To do this, we utilized SPT-TIRF on CXCR4-deficient Jurkat cells ($JK^{-/-}$) transiently transfected with CXCR4 fused to the AcGFP monomeric protein (CXCR4-AcGFP) and pretreated or not with the selected small compounds (50 μM, 45 minutes, 37ºC). The compounds had no effect on unstimulated cells, and we observed mainly receptor monomers and dimers (~85–91%), with a very low percentage of complexes with more than three receptors (~9–16%) (Fig. 2A). Accordingly, the basal mean spot intensity (MSI) of CXCR4 was very similar in all cases (~1,500 a.u.) (Fig. 2B). Under these experimental conditions, most of the particles corresponded to mobile particles (~87%) (Fig. 2C), and none of the selected compounds affected the short time-lag diffusion coefficient (D_{1-4}) for CXCR4 trajectories, with a median value of ~0.02 $\mu m^2/s$ (Fig. 2D).

We next examined how pre-treatment with the selected compounds affected receptor dynamics upon CXCL12 stimulation. Pretreatment with AGR1.135 and AGR1.137, but not with AGR1.131, substantially impaired CXCL12-mediated receptor nanoclustering (46–60% of nanoclusters with ≥3 receptors/particle in untreated and in AGR1.131-treated cells *versus* 15–16% in cells pretreated with AGR1.135 or AGR1.137) (Fig. 2A), with an MSI of 3,002 a.u. for CXCR4 in untreated cells and 3,618 a.u. in AGR1.131-treated cells *versus* 1,611 a.u. in AGR1.135- and 1,403 a.u. in AGR1.137-treated cells (Fig. 2B). The effect was also evident when we evaluated the dynamic parameters of CXCR4. In control cells (untreated or AGR1.131-treated cells), CXCL12 significantly increased the percentage of immobile particles (12% in untreated cells *versus* 24% in untreated cells + CXCL12 and 20% in AGR1.131-treated cells + CXCL12) (Fig. 2C), whereas AGR1.135 and AGR1.137 pretreatment had no effect on the percentage of immobile particles after CXCL12 stimulation (14% for AGR1.135 and 16% for AGR1.137). Moreover, the expected reduction in CXCR4 diffusivity triggered by CXCL12 in untreated (median $D_{1-4} = 0.0086\ \mu m^2\ s^{-1}$) or AGR1.131-treated (median $D_{1-4} = 0.0099\ \mu m^2\ s^{-1}$) cells was abolished with AGR1.135 ($D_{1-4} = 0.0169\ \mu m^2\ s^{-1}$) and AGR1.137 ($D_{1-4} = 0.0165\ \mu m^2\ s^{-1}$) treatments (Fig. 2D).

Altogether, these results suggest that AGR1.135 and AGR1.137 behave as allosteric antagonists of CXCR4 and alter the CXCL12-mediated receptor nanoclustering and dynamics.

AGR1.135 and AGR1.137 incompletely abolish CXCR4-mediated responses in Jurkat cells

CXCR4 internalizes in response to CXCL12, a process that mediates receptor desensitization (26). Our previous results indicate that CXCR4 nanoclustering and internalization are independent processes (20). Indeed, CXCL12 triggers normal CXCR4mut internalization but fails to promote receptor nanoclustering (20). We thus tested whether the selected antagonists

affected CXCL12-mediated CXCR4 internalization. Jurkat cells treated with vehicle or the selected compounds (50 μM, 30 minutes, 37ºC) were stimulated with CXCL12 (50 nM, 37ºC) and receptor internalization was evaluated by flow cytometry using anti-CXCR4 antibodies. Neither AGR1.135 nor AGR1.137 treatment altered the internalization of CXCR4 that was observed in untreated Jurkat cells or in AGR1.131-treated cells (Fig. 3A). These data suggest that none of the antagonists alters CXCL12 binding to CXCR4, which supports the *in silico* screening strategy to preserve ligand-binding integrity. Indeed, using flow cytometry analysis and CXCL12-ATTO 700 (27) we confirmed that none of the selected compounds affected ligand binding, whereas this was blocked by the ligand-binding inhibitor AMD3100 (Fig. 3B, Supplementary Fig. 2).

Because CXCL12 promotes Gi-protein activation, we analyzed the effects of the selected compounds on CXCL12-mediated inhibition of cAMP production, a canonical signaling pathway downstream of CXCR4 activation. In contrast to the effect promoted by AMD3100, a binding-site antagonist of CXCR4, none of the compounds altered CXCL12-mediated Gi protein activation (Fig. 3C). We next evaluated their effects on other signaling pathways such as ERK1/2 phosphorylation and PI3K activation (28). Jurkat cells treated with vehicle or the selected compounds (50 μM, 30 minutes, 37ºC) were activated with CXCL12 (50 nM) for different time periods and cell lysates were analyzed by western blotting using anti-P-ERK1/2 and -P-AKT antibodies. Neither AGR1.135 nor AGR1.137 nor control AGR1.131 treatments blocked CXCL12-mediated activation of the two signaling pathways (Fig. 3D, Supplementary Fig. 3). Overall, these data indicate that although the selected compounds inhibit CXCL12-induced chemotaxis in Transwell assays, they do not impact G-protein activation or other ligand-mediated signaling pathways such as ERK1/2 or PI3K.

Alterations in actin cytoskeleton dynamics are linked to deficiencies in ligand-mediated receptor nanoclustering and to defects in the ability of cells to sense chemoattractant gradients. Cells treated with latrunculin A, an actin polymerization inhibitor (20), and cells expressing CXCR4WHIM^{R334X}, which fail to correctly control actin dynamics (21, 29), have defective CXCL12-mediated nanoclustering and were unable to appropriately sense chemoattractant gradients. Using flow cytometry and phalloidin staining on Jurkat cells treated with vehicle or the selected compounds (50 μM, 37ºC), we detected altered actin polymerization in cells treated with AGR1.135 and AGR1.137 (Fig. 4A). Data were corroborated by immunostaining and confocal analysis. Whereas Jurkat cells treated with vehicle or AGR1.131 were correctly polarized after CXCL12 activation, AGR1.135 and AGR1.137 treatments promoted a reduction in the number of polarized cells (Fig. 4B). As control, AGR1.137 did not affect anti-CD3 mediated actin polymerization, discarding a direct effect of the compound on actin or actin-binding proteins (Supplementary Fig. 4).

CXCR4 nanoclustering has been recently associated with the migratory phenotype of T cell blasts (21, 29). To explore how the antagonists affected the phenotype of migrating cells, we added T cell blasts previously treated with vehicle or with the selected compounds (50 μM, 30 minutes, 37ºC) to a 2D-lipid bilayer system with embedded ICAM-1, alone or with CXCL12. We observed that treatment with AGR1.135 and AGR1.137, but not with AGR1.131, abolished CXCL12-induced cell migration and cell adhesion (Fig. 4C, D).

Given that the antagonistic effects of AGR1.135 and AGR1.137 are also compatible with a partial agonist behavior, we used Transwell chambers to evaluate the ability of the selected compounds to promote Jurkat cell migration. None of the compounds induced cell migration (Supplementary Fig. 5). Overall, our results suggest that AGR1.135- and AGR1.137-driven modulation of CXCR4 nanoclustering blocks certain receptor-associated functions, including actin dynamics, directed-cell migration, integrin-mediated adhesion and migration, whereas other functions remain unaffected (i.e., receptor internalization, inhibition of cAMP production and ERK1/2 activation).

AGR1.135 and AGR1.137 antagonists act by direct binding on CXCR4

We failed to detect a direct interaction between the compounds and CXCR4; therefore, we tried an indirect approach. By *in silico* MD analysis using AMBER14, we defined those CXCR4

residues involved in binding of the compounds, and generated point mutant receptors to determine the inhibitory effect of AGR1.135, AGR1.137 and AGR1.131 (control) on CXCL12-mediated chemotaxis. We initially performed a binding-site search using PELE software, a Monte Carlo-based technique (30), to identify the most promising CXCR4 binding sites of the selected compounds. AGR1.135 and AGR1.137 showed one of the most stable trajectories upon binding to the cleft formed by TMV and TMVI (Fig. 5A-C). By contrast, the most stable trajectories for AGR1.131 (control) corresponded to the binding to a contiguous region localized between TMI and TMVII (Fig. 5D). Once the binding site of the compounds was confirmed, we performed docking studies to discern the best poses as a starting point for additional studies.

Results showed that AGR1.135 and AGR1.137 shared a similar binding mode (Fig. 5A) and might interact with CXCR4 in a molecular cavity between TMV and TMVI. Specifically, AGR1.135 established hydrogen bonds with residues G207, Y256 and R235, although in the latter case, a pi-cation interaction was also possible (Fig. 5B, Supplementary Fig. 6A). Additionally, AGR1.135 could interact hydrophobically with several residues in TMV and TMVI comprising a total surface of 400 $Å^2$ with a length of 20 Å (Fig. 5B). AGR1.137 might use the carboxyl group of V124 in TMIII and overlap with AGR1.135 binding in the cavity, interacting with the other 19 residues scattered between TMV and VI to create an interaction surface of 370 $Å^2$ along 20 Å (Fig. 5C; Supplementary Fig. 6B). AGR1.137 did not have the phenyl ring present in AGR1.135, likely explaining why it did not interact with the residue R235 (Fig. 5C). Regarding AGR1.131, its best binding site was the pocket between helices TMI and TMVII (Fig. 5D), which is likely the reason why this compound had no effect on receptor oligomerization.

To confirm the putative binding sites for AGR1.135 and AGR1.137, we generated several point mutations in CXCR4 using the residues identified in each case that did not interfere with signal transduction: G207I, L208K, R235L, F249L and Y256F. Additionally, we also added the mutations I204K, S260A as controls, as they are included in the same area (TMV-TMVI cleft) but did not interfere with compound binding or the CXCL12 binding site. All CXCR4 mutants were normally expressed at the cell surface, as demonstrated by flow cytometry (Supplementary Fig. 7), and were fully functional, as evidenced in a CXCL12-mediated cell chemotaxis assay~~s~~ (Fig. 6A).

We next used transient transfection of $JK^{-/-}$ cells with each of the mutants or with wild-type CXCR4, which were treated with vehicle, AGR1.135 or AGR1.137 (50 μM, 30 minutes, 37ºC) prior to assessing migration towards CXCL12 gradients in Transwell chambers. The antagonistic effect of AGR1.135 was reverted in cells transfected with the CXCR4 plasmid carrying the specific point mutations L208K or Y256F (Fig. 6B). Similarly, the antagonistic effect of AGR1.137 was reverted in cells expressing L208K, Y256F or F249L mutants (Fig. 6B). Overall, these data indicate that the selected compounds directly bind to CXCR4, that the L208K and Y256F residues in the CXCR4 TMVI domain are critical for the antagonistic activities of AGR1.135 and AGR1.137 and that F249L is also important for the effect of AGR1.137.

AGR1.137 treatment reduces tumor volume and dissemination in a zebrafish xenograft model

Finally, to ascertain the *in vivo* activity of the selected compounds, we considered the role of CXCR4 in tumor growth and metastasis (10, 15) and the transparency of zebrafish larvae to develop a tumor xenograft (ZTX) model. ZTX models have emerged as a powerful complementary *in vivo* system for research in oncology and tumor biology (31, 32), particularly for early tumor invasion and dissemination.

We used HeLa cells, which are derived from a human cervical tumor that expresses a functional CXCR4 (Fig. 7A, B; Supplementary Fig. 8A), and which have been previously used in ZTX models (33, 34). HeLa cells respond to CXCL12 gradients in directed-cell migration assays (Fig. 7A, B) and, as occurred in Jurkat cells, their treatment with AGR1.137 but not with AGR1.131 (control) abrogated directed-cell migration towards a CXCL12 gradient (Fig. 7A, B, Supplementary video 1-4). As control of specificity, AGR1.137 treatment did not affect CXCL2-mediated direct HeLa cell migration whereas it was blocked by the specific CXCR2 inhibitor AZD5069 (Fig. 7C,D).

DiI-labeled HeLa cells, treated with vehicle, AGR1.135, AGR1.137 or AGR1.131 (control), were implanted subcutaneously in the perivitelline space of 2-day-old zebrafish larvae. Images of each tumor-bearing larva were taken immediately after implantation and 3 days later, and the relative change in tumor size was determined. AGR1.135 was discarded as most of the treated larvae died, indicating a toxic effect. By contrast, AGR1.137 was not toxic to embryos, and no other non-lethal toxic phenotypes (e.g., pericardial edema, head and tail necrosis, malformation of the head or tail, brain hemorrhage or yolk sac edema) were evident; and it was not teratogenic. AGR1.137 markedly reduced the size of high-intensity red fluorescent tumors, whereas the control AGR1.131 had no effect on tumor size as compared with vehicle-treated fish, and AMD3100 reduced tumor size to a similar extent as AGR1.137 (Fig. 7E). These data clearly show an antiproliferative effect of AGR1.137 on HeLa cells. As a control, AGR1.137 also reduced HeLa cell proliferation in *in vitro* assays mimicking the *in vivo* experimental conditions in Zebrafish (addition of compounds every 24 hours for 3 days) (Supplementary Fig. 8B). We next evaluated the ability of the compounds to block cell dissemination by determining the number of labeled HeLa cells that emerged in the main metastatic niche at the caudal hematopoietic plexus. AGR1.137 treatment of HeLa cells reduced cell dissemination by 50% (Fig. 7F), strongly suggesting that this compound exerts anti-metastatic effects. The combined ability of AGR1.137 to reduce proliferation and dissemination *in vivo* likely holds therapeutic value.

Discussion

The CXCL12/CXCR4 axis is involved in myriad functions including leukocyte recruitment, embryogenesis, vascular development, hematopoiesis, heart development, nervous system organization, tumor progression, autoimmune diseases and, together with CD4, CXCR4 is a co-receptor used by the HIV-1 virus to infect immune cells (35). This evidence supports the clinical interest in developing specific antagonists to modulate or directly block CXCR4 functions.

Plerixafor (AMD3100), which blocks ligand binding, is the first FDA-approved CXCR4 antagonist used for peripheral blood stem cell transplantation regimens (36). Unfortunately, its clinical application is limited by poor pharmacokinetics and adverse effects associated with long-term administration (37, 38). These limitations and the poor clinical success of other chemokine receptor antagonists have prompted the search for alternative strategies to block chemokine receptor functions.

As for other GPCRs, CXCR4 exists in the plasma membrane in multiple conformations and interacts with other chemokine receptors (39) and also with cell surface proteins such as the T-cell receptor (40), CD4 and other receptors (20, 35). Advanced imaging-based techniques such as SPT-TIRF and super-resolution microscopy have revealed the presence of CXCR4 monomers, dimers and oligomers at the cell membrane that diffuse as nanoclusters in the lipid bilayer. CXCL12 binding triggers receptor nanoclustering and reduces the percentage of monomers and dimers. This effect is essential for the full activation of the CXCR4 signaling pathway and the correct orientation of the cell towards chemokine gradients (20, 21, 29). For instance, $CXCR4R^{334X}$, a truncated mutant receptor causing WHIM syndrome, fails to form nanoclusters in the presence of CXCL12 and is unable to sense chemoattractant gradients, although it remains able to trigger Ca^{2+} flux and other signaling pathways (21). Due to the inability to connect CXCR4 with the actin cytoskeleton, β-arrestin-1-deficient cells do not exhibit CXCL12-mediated receptor nanoclustering (21). Similar observations are seen with cells expressing CXCR4 and treated with latrunculin A, an actin polymerization inhibitor (20, 35). Altogether, these observations indicate that receptor nanoclustering is a ligand-mediated process, requiring activation of a signaling pathway involving β-arrestin-1 and correct actin cytoskeleton dynamics.

CXCR4 contains a pocket created by two TM segments, TMV and TMVI, and mutations in this pocket can affect the dynamics of the conformational changes triggered by ligand binding. The mechanism involves the initial interaction of CXCL12 with the extracellular region of CXCR4, which promotes conformational changes to a series of hydrophobic residues present mostly on TMV and

TMVI that continue downwards in the TM domains of the receptor, ultimately allowing G-protein interaction and activation (22). Interestingly, a complete GPCR class A chemokine receptor alignment reveals that hydrophobic residues in this area that are not in highly conserved positions could present any side-chain length in any site depending on the receptor, which likely confers a specificity that could be exploited for the discovery and/or design of new antagonists (41) (Supplementary Fig. 9).

To identify new allosteric antagonists with reduced potential side-effects, we focused on an *in silico* screening directed to the pocket in CXCR4 created by TMV and TMVI, without affecting the residues involved in CXCL12 binding (20, 35). Subsequent functional analysis of the selected compounds identified AGR1.135, AGR1.137, and AGR1.131. The latter, although selected with the same *in silico* criteria, did not block CXCL12-mediated chemotaxis. In addition, the compounds did not affect neither CXCR2-mediated cell migration, supporting their specificity for CXCR4. The three compounds had a common core of (4-(1-benzyl-1H-1,2,3-triazol-4-yl)phenyl)methanol but distinct side chains that carry amines of different length and chemical nature, which might explain their different biological activity.

SPT-TIRF analysis indicated that AGR1.135 and AGR1.137 abolished the ability of CXCL12 to trigger CXCR4 nanoclustering and altered the receptor dynamics at the cell membrane. Moreover, as expected from the selection criteria, these compounds did not alter CXCL12 binding, receptor internalization, inhibition of cAMP-production or ERK1/2 or PI3K activation. The results also suggested the existence of distinct CXCR4 conformational states responsible for the activation of different signaling pathways. It is well known that GPCRs are thought to reside in the plasma membrane in equilibrium between distinct states, depending on complex allosteric interactions and conformational changes promoted by ligands, as well as on cell-specific parameters (42, 43). Many GPCRs show basal activity that can be modulated by ligands with different efficacy. Full agonists can induce the maximal signaling response, whereas partial agonists and inverse agonists promote submaximal signaling or decrease basal activity, respectively. In addition, some ligands are known to be biased because they selectively activate specific receptor-associated pathways at the expense of others, supporting the presence of distinct receptor conformations (44). Studies on the β2-adrenergic receptor reinforce the idea that distinct agonists stabilize different receptor conformations (45), raising the possibility that allosteric ligands shift the equilibrium to favor a particular receptor conformation.

CXCR4 docking studies to refine the binding mode of the selected compounds combined with a point mutation strategy confirmed the binding specificity of the antagonists. AGR1.135 and AGR1.137 lost their antagonism on cells expressing CXCR4L208K or CXCR4Y256F. In addition, the inhibitory behavior of AGR1.137 was also missed in cells expressing CXCR4F249L. Both antagonists showed stable trajectories bound to CXCR4, being able to occupy the cavity formed by TMV and TMVI and keeping specific hydrogen bond interactions and hydrophobic contacts along the interaction surface. Moreover, there were differences between the two antagonists in terms of binding; whereas AGR1.135 had a stronger interaction due to three hydrogen bonds that curved the position of the molecule as it fitted into the cavity formed by TMV and TMVI, AGR1.137 bound to the carboxyl group of V124 in TMIII, penetrating deeper into the receptor and then following the TMV–TMVI cleft down to the bottom of the cavity. In both cases, hydrophobic interactions with several residues of the receptor allowed the compounds to attach to the cleft and partially abrogate the movement of TMVI required for complete signal transmission (22). These differences might explain the distinct behavior of both compounds on cells expressing CXCR4F249L and suggest a closer interaction between the triazole group of AGR1.137 and the F249 residue on CXCR4. The region has also been implicated in the connection of the orthosteric chemokine binding pocket to the lipid bilayer. These observations highlight the flexibility of the cavity and its potential for modulation. They also suggest that this cavity could be used to guide the development of a new generation of antagonists that, without affecting CXCL12 binding, allosterically modulate some GPCR-mediated functions without altering others.

CXCR4 overexpression contributes to tumor growth, invasion, angiogenesis, metastasis, relapse and therapeutic resistance (46). As might be expected, CXCR4 antagonism has been

shown to disrupt tumor-stromal interactions, sensitize cancer cells to cytotoxic drugs, and reduce tumor growth and metastatic burden (46). We used a ZTX model with HeLa cells, which express functional CXCR4, to evaluate the *in vivo* relevance of the selected antagonists. This is a well-studied model to evaluate tumor progression and metastasis (33). Our results demonstrate that AGR1.137 treatment of HeLa cells reduces the relative tumor size by 50% and limits cell dissemination in the absence of toxicity, altogether indicating that this compound has both anti-proliferative and anti-metastatic properties. While the effect of AGR1.137 on cell dissemination could be a consequence of its impact on tumorigenesis, it also abolished *in vitro* directed-HeLa cell migration, supporting the inhibition of cell metastasis.

Our data support the notion of CXCR4 as a flexible protein that can adopt a spectrum of conformations depending on several factors such as the presence of a bound ligand, the lipid composition of the cell membrane (29) and the presence of other interacting proteins. As for many GPCRs, the stabilization of distinct CXCR4 states is a key element to modulate its function (47, 48). Our data show that by targeting the pocket between TMV and TMVI in CXCR4, AGR1.137 can block (both *in vitro* and *in vivo*) CXCL12-mediated receptor nanoclustering and cell sensitivity towards chemoattractant gradients without altering ligand binding and, thus, preserving other signaling events. Ultimately, these results demonstrate the value in stabilizing specific CXCR4 conformations and in considering targets other than the ligand-binding site for the design of partial antagonists with reduced side-effects to block a specific set of CXCR4 functions.

Materials and Methods

Cells and reagents

HeLa cells were obtained from the American Type Culture Collection (CCL-2; Rockville, MD). Jurkat human leukemia $CD4^+$ cells were kindly provided by Dr. J. Alcamí (Centro Nacional de Microbiología, Instituto de Salud Carlos III, Madrid, Spain) and BAF/3-$CCR4^+$ cells by Dra. L. Kremer (Centro Nacional de Biotecnología/CSIC, Madrid, Spain). Where indicated, Jurkat cells lacking endogenous *CXCR4* expression ($JK^{-/-}$) (21) were transiently transfected with plasmids expressing wild-type or mutant CXCR4-AcGFP receptors (20 μg), as described (21). CXCR4 mutants were generated by PCR using the QuikChange site-directed mutagenesis kit (Stratagene, La Jolla, CA) with full-length CXCR4-AcGFP serving as a template and specific primers (Supplementary Table 2).

Human peripheral blood mononuclear cells isolated from buffy coats were activated *in vitro* for 1 week with 20 U/mL of IL-2 (Teceleukin; Roche, Nutley, NJ) and 5 μg/mL phytohemagglutinin (Roche) to generate T cell blasts (29).

The following antibodies were used: monoclonal mouse anti-human CXCR4 (clone 44717) and phycoerythrin-conjugated human CXCR4 (clone 12G5; both from R&D Systems, Minneapolis, MN); purified mouse anti-human CD3 (clone HIT3a, BD Biosciences, Franklin Lakes, NJ); goat F(ab')2 anti-mouse IgG-PE (Southern Biotech, Birmingham, AL); and anti-phospho-AKT (Ser473), anti-AKT (#9272), anti-phospho-ERK1,2 (#9191) and anti-ERK (#9102) (all from Cell Signaling Technology, Danvers, MA). Human CXCL12, CXCL2 and CCL17 were obtained from PeproTech (Rocky Hill, NJ). Human CXCR4 was cloned into the pAcGFPm-N1 plasmid (Clontech Laboratories, Palo Alto, CA), as described (20).

Unless otherwise indicated, cells were pre-treated with 50 μM of the selected small compounds, 10 μM AMD3100 (Merck, Darmstadt, Germany), 1 μM AZD5069 (MedChemExpress, Monmouth Junction, NJ) or vehicle (DMSO) as control (30 minutes, 37°C, 5% CO_2).

Binding experiments were performed using CXCL12-Atto-700 (27), kindly donated by Prof. Marcus Thelen (Institute for Research in Biomedicine, Università della Svizzera italiana, Bellinzona, Switzerland).

Compounds database

All the compounds used in the present study were synthesized in the Centro de Investigaciones Biológicas Margarita Salas (CIB-CSIC, Madrid) following previously described procedures (49). Synthetic and analytical data are shown as Supplementary information. All the compounds have a purity ≥95% determined by high-performance liquid chromatography. Compounds are collected in the Medicinal and Biological Chemistry (MBC) library (CIB-CSIC) (24), which contains more than 2,000 drug-like compounds.

Discovery of CXCR4 modulators

The CXCR4 model was built on the SWISS-MODEL server (25) using the human CXCR4 sequence and the crystallographic structure of a CXCR4 dimer in complex with the small molecule IT1t as template (PDB code: 3ODU) (50). The model was further optimized by adding hydrogens, ionizing the structure at pH 7.2, and adjusting size chain positions using the Maestro Protein Preparation Wizard tool included in the Schrödinger software package (51). Virtual screening of ligands was performed from the compounds included in the MBC library using the "Glide" module as a docking tool on CXCR4 model. Optimization of the ligand-binding regions was performed using the script "Unconstrained ligand exploration and binding search" of the Protein Energy Landscape Exploration (PELE) program (30), yielding 20 PELE trajectories for each ligand. The CXCR4-IT1t complex was used as a control to validate the protocol. In order to obtain initial poses for Molecular Dynamics (MD) simulations, additional docking studies were performed in Autodock v4.2 (52) using a grid box that contained the intracellular portion of the protein. The CXCL12 binding pocket was excluded from the search and the most promising docking poses were further studied using MD simulations to determine their stability and interactions with the receptor. Simulations were performed using AMBER14 (53) with ff14SB (54) and lipid14 (55) force fields in the NPT thermodynamic ensemble (constant pressure and temperature); 50-ns MD simulations without position restraints were calculated using a time step of 2 fs. Trajectories of the most interesting poses were extended to 150 ns. To estimate the affinity of the ligands for CXCR4, the binding energy of each representative structure obtained with the principal components analysis was calculated using the PRODIGY-LIGAND server (56).

Transwell migration assay

Cells (3×10^5) in 0.1 ml of RPMI medium containing 10 mM HEPES and 0.1% BSA were placed in the upper wells of 5 μm pore size transmigration chambers (Transwell, Costar, Corning, NY). CXCL12 (12.5 nM) or CCL17 (50nM) in 0.6 ml of the same medium was added to the lower well. Cell migration was evaluated as described (21).

Cell cycle analysis

Cells (5×10^5 cells/well) were collected from microplates and washed twice in PBS and then resuspended in 50 μl of detergent (DNA-Prep Reagent Kit; Beckman Coulter, Brea, CA) containing 10 ng/ml propidium iodide (DNA-Prep Reagent Kit; 30 minutes, 37°C). Cell cycle phases were analyzed by flow cytometry on a Beckman Coulter FC500 flow cytometer and results were expressed as the percentage of stained cells.

Single molecule TIRF imaging and analysis

Transfected cells expressing 8,500–22,000 receptors/cell (<4.5 particles/μm^2) were selected for detection and tracking analysis. Experiments were performed at 37ºC with 5% CO_2 using a total internal reflection fluorescence (TIRF) microscope (Leica AM TIRF inverted microscope; Leica Microsystems, Wetzlar, Germany). Image sequences of individual particles (500 frames) were then acquired at 49% laser power (488-nm diode laser) with a frame rate of 10 Hz

(100 ms/frame). The penetration depth of the evanescent field was 90 nm. Particles were detected and tracked using the U-Track2 algorithm (57) implemented in MATLAB, as described (58). Mean spot intensity (MSI), number of mobile and immobile particles and diffusion coefficients (D_{1-4}) were calculated from the analysis of thousands of single trajectories over multiple cells (statistics provided in the respective figure captions) using described routines (58). The receptor number along individual trajectories were determined as reported (20), using the intensity of the monomeric protein CD86-AcGFP as a reference. Values were confirmed using single-step photobleaching analysis.

Internalization and flow cytometry studies

Cells (5×10^5 cells/well) were activated with CXCL12 (50 nM) at the indicated time points. After incubation, cells were washed twice with staining buffer and receptor internalization was determined by flow cytometry using an anti-CXCR4 mAb (clone 44717, 30 minutes, 4°C), followed by secondary staining with PE-coupled goat anti-mouse IgG (30 min, 4ºC). Results are expressed as a percentage of the mean fluorescence intensity of treated cells relative to that of unstimulated cells.

Western blotting

Cells (3×10^6) were activated with CXCL12 (50 nM) at the time points indicated and then lysed in RIPA detergent buffer supplemented with 1 mM PMSF, 10 μg/mL aprotinin, 10 μg/mL leupeptin and 10 μM sodium orthovanadate, for 30 minutes at 4ºC. Extracts were analyzed by western blotting using specific antibodies. Densitometric evaluation of blots was performed using ImageJ (NIH, Bethesda, MD).

cAMP determination

cAMP levels were determined using the cAMP-Glo™ Max Assay (Promega, Madison, WI, in cells (5×10^5 cells/well) untreated or pre-treated with CXCL12 (50 nM, 5 minutes, 37°C) followed by the addition of forskolin (10 μM, 10 minutes, 37°C).

CXCL12 binding

Cells (5×10^5 cells/well) were incubated with CXCL12 ATTO-700 (27), (30 minutes, 37°C) and maintained at 4°C before analyzing the bound fluorescence in a Beckman Coulter Cytoflex flow cytometer. Results are expressed as mean fluorescence intensity.

Actin polymerization

Cells (5×10^5 cells/well) were incubated with CXCL12 (50 nM, 37°C) or anti-CD3 (1 μg/ml, 37°C) at the indicated time periods and then fixed with 2% paraformaldehyde and transferred to ice for 10 minutes. Fixed cells were permeabilized with 0.01% saponin (10 minutes, 4ºC) and labeled with Phalloidin-TRITC (Merck, 30 minutes, 4ºC). After washing, bound fluorescence was analyzed by flow cytometry on a Beckman Coulter FC500 flow cytometer.

Immunofluorescence analyses

Cells on fibronectin (20 μg/ml, Sigma)-coated glass slides were stimulated or not with 100 nM CXCL12 (5 minutes at 37 °C), fixed with 4% paraformaldehyde (10 minutes), permeabilized with 0.25% saponin (10 minutes), and stained with phalloidin-TRITC (Sigma-Merck; 30 minutes), all at room temperature (RT). Preparations were analyzed using a Leica TCS SP8 confocal multispectral microscope.

Cell adhesion/migration on planar lipid bilayers

Planar lipid bilayers were prepared as reported (59). Briefly, unlabeled GPI-linked intercellular adhesion molecule 1 (ICAM-1) liposomes were mixed with 1,2-dioleoyl-phosphatidylcoline. Membranes were assembled in FCS2 chambers (Bioptechs, Butler, PA), blocked with PBS containing 2% FCS for 1 hour at RT, and coated with CXCL12 (200 nM, 30 minutes, RT). Cells (3×10^6 cells/ml) in PBS containing 0.5% FCS, 0.5 g/l D-glucose, 2 mM $MgCl_2$ and 0.5 mM $CaCl_2$ were then injected into the pre-warmed chamber (37ºC). Confocal fluorescence, differential interference contrast (DIC) and interference reflection microscopy (IRM) images were acquired on a Zeiss Axiovert LSM 510-META inverted microscope with a 40× oil-immersion objective. Imaris 7.0 software (Bitplane, Zurich, Switzerland) and ImageJ 1.49v were used for qualitative and quantitative analysis of cell dynamics parameters, fluorescence and IRM signals. The fluorescence signal of the planar bilayer in each case was established as the background fluorescence intensity. The frequency of adhesion (IRM^+ cells) per image field was estimated as [nº of cells showing IRM contact/total nº of cells (estimated by DIC)] × 100; similarly, we calculated the frequency of migration (cells showing and IRM contact and moving over time).

Directional cell migration

Pre-treated cells were diluted to 10×10^6 cell/ml in RPMI medium containing 1% BSA and 20 mM HEPES (chemotaxis medium), seeded into the channel of a chemotaxis slide (μ-Slide Chemotaxis System, 80326; Ibidi, Munich, Germany) (1 hour, 37ºC, 5% CO_2). The reservoirs were then filled with chemotaxis medium containing 50 μM AGR1.137 or AGR1.131, or vehicle (DMSO) as a control condition, and 100 nM CXCL12 or CXCL2 was added to the right reservoir. Phase-contrast images were recorded over 20 hours with a time lapse of 15 minutes using a Microfluor inverted microscope (Leica) with a 10× objective and equipped with an incubation system set to 5% CO_2 and 37°C. Single-cell tracking was evaluated by selecting the center of mass in each frame using the manual tracking plug-in tool in ImageJ software. Spider plots, representing the trajectories of the tracked cells, forward migration index (FMI), and straightness values, were obtained using the Chemotaxis and Migration Tool (ImageJ software).

Drug efficacy assay in zebrafish

HeLa cells were labeled with 8 μg/ml Fast-DiI™ oil (Cat #D3899; ThermoFisher Scientific, Waltham, MA) in RPMI medium supplemented with 2% FBS for 30 minutes at 37°C. Cells were then washed and filtered, and cell viability was determined using trypan blue-exclusion. Transgenic zebrafish Tg(fli1a:EGFP)y1 (60) were bred naturally and maintained in E3 embryo medium (deionized water containing NaCl 0.5 mM, $CaCl_2$ 0.4 mM, MgSO4 0.7 mM and KCl 0.2 mM, pH 7.2) supplemented with 0.2 mM PTU (E3/PTU) at 28.5°C. DiI-labeled HeLa cells were implanted in the dorsal perivitelline space of 2-day-old embryos, as described (31). Tumors were imaged within 2 hours of implantation and tumor-baring embryos were treated with either vehicle (DMSO), AMD-3100 or with AGR1.131 or AGR1.137 (50 μM) for three days, followed by re-imaging. Changes in tumor size were evaluated as tumor area at day 3 divided by tumor area at day 0, and metastasis was evaluated as the number of cells disseminated to the caudal hematopoietic plexus.

Statistical analyses

All data were analyzed with GraphPad Prism software version 9 (GraphPad Inc., San Diego, CA). Cell migration in Transwell assays and in planar lipid bilayers and directional cell migration assays and cell polarization under the various conditions were analyzed to determine significant differences between means using one-way analysis of variance (ANOVA) followed by Tukey's multiple comparison test. A two-tailed Mann-Whitney non-parametric test was used to analyze the diffusion coefficient (D_{1-4}) of single particles. We used contingency tables to compare two or more groups of categorical variables, such as the percentages of mobile or immobile particles, and these were compared using a Chi-square test with a two-tailed p-value. Statistical

differences were reported as n.s. = not significant $p > 0.05$, *$p \leq 0.05$, **$p \leq 0.01$, ***$p \leq 0.001$ and ****$p \leq 0.0001$.

Acknowledgments

This work was supported by grants from the Spanish Ministry of Science and Innovation (PID2020-114980RB-I00). NEC is supported by a grant of the Spanish Ministry of Economy, Industry and Competitivity (RTI2018-096100B-100). RJS is supported by FSE/FEDER through the Instituto de Salud Carlos III (ISCIII; CP20/00043). EG-C was supported by the program Apoyos Centros de Excelencia S.O. of the Spanish Ministry of Science and Innovation (SEV-2017-0712). PM and SG are included in the doctoral program of the Department of Molecular Biosciences, Universidad Autónoma de Madrid, and are supported by the Fondo de Personal Investigador (FPI) program of the Spanish Ministry for Science and Innovation (BES2015-071302 and PRE2018-083201 respectively). RA-B is supported by the Garantía Juvenil program of the Regional Government of Madrid, Spain (CAM20_CNB_AI_07).

We also acknowledge the technical help of the Advance Light Microscopy Unit at the CNB/CSIC. Compounds AGR1.31, AGR1.35 and AGR1.37 are included in the patent PCT/ES2022/070379.

References

1. A. Zlotnik, O. Yoshie, The chemokine superfamily revisited. *Immunity* **36**, 705–716 (2012).

2. Y. Nie, Y. C. Han, Y. R. Zou, CXCR4 is required for the quiescence of primitive hematopoietic cells. *J Exp Med* **205**, 777–783 (2008).

3. D. E. Wright, E. P. Bowman, A. J. Wagers, E. C. Butcher, I. L. Weissman, Hematopoietic stem cells are uniquely selective in their migratory response to chemokines. *J Exp Med* **195**, 1145–1154 (2002).

4. T. Lapidot, O. Kollet, The essential roles of the chemokine SDF-1 and its receptor CXCR4 in human stem cell homing and repopulation of transplanted immune-deficient NOD/SCID and NOD/SCID/B2m(null) mice. *Leukemia* **16**, 1992–2003 (2002).

5. H. E. Broxmeyer, *et al.*, Stromal cell-derived factor-1/CXCL12 directly enhances survival/antiapoptosis of myeloid progenitor cells through CXCR4 and G(alpha)i proteins and enhances engraftment of competitive, repopulating stem cells. *J Leukoc Biol* **73**, 630–638 (2003).

6. T. Cash-Padgett, A. Sawa, H. Jaaro-Peled, Increased stereotypy in conditional Cxcr4 knockout mice. *Neurosci Res* **105**, 75–79 (2016).

7. K. Tachibana, *et al.*, The chemokine receptor CXCR4 is essential for vascularization of the gastrointestinal tract. *Nature* **393**, 591–594 (1998).

8. Y. Takabatake, *et al.*, The CXCL12 (SDF-1)/CXCR4 axis is essential for the development of renal vasculature. *J Am Soc Nephrol* **20**, 1714–1723 (2009).

9. E. A. Berger, P. M. Murphy, J. M. Farber, Chemokine receptors as HIV-1 coreceptors: roles in viral entry, tropism, and disease. *Annu Rev Immunol* **17**, 657–700 (1999).

10. A. Müller, *et al.*, Involvement of chemokine receptors in breast cancer metastasis. *Nature* **410**, 50–56 (2001).

11. J. M. Hall, K. S. Korach, Stromal cell-derived factor 1, a novel target of estrogen receptor action, mediates the mitogenic effects of estradiol in ovarian and breast cancer cells. *Mol Endocrinol* **17**, 792–803 (2003).

12. R. S. Taichman, *et al.*, Use of the stromal cell-derived factor-1/CXCR4 pathway in prostate cancer metastasis to bone. *Cancer Res* **62**, 1832–1837 (2002).

13. S. Scala, *et al.*, Human melanoma metastases express functional CXCR4. *Clin Cancer Res* **12**, 2427–2433 (2006).

14. H. Geminder, *et al.*, A possible role for CXCR4 and its ligand, the CXC chemokine stromal cell-derived factor-1, in the development of bone marrow metastases in neuroblastoma. *J Immunol* **167**, 4747–4757 (2001).

15. A. Orimo, *et al.*, Stromal fibroblasts present in invasive human breast carcinomas promote tumor growth and angiogenesis through elevated SDF-1/CXCL12 secretion. *Cell* **121**, 335–348 (2005).

16. Z. Liang, *et al.*, CXCR4/CXCL12 axis promotes VEGF-mediated tumor angiogenesis through Akt signaling pathway. *Biochem Biophys Res Commun* **359**, 716–722 (2007).

17. O. L. Bohn, *et al.*, Biomarker profile in breast carcinomas presenting with bone metastasis. *Int J Clin Exp Pathol* **3**, 139 (2010).

18. S. Y. Kim, *et al.*, Inhibition of the CXCR4/CXCL12 chemokine pathway reduces the development of murine pulmonary metastases. *Clin Exp Metastasis* **25**, 201–211 (2008).

19. E. De Clercq, Mozobil® (Plerixafor, AMD3100), 10 years after its approval by the US Food and Drug Administration. *Antivir Chem Chemother* **27** (2019).

20. L. Martínez-Muñoz, *et al.*, Separating Actin-Dependent Chemokine Receptor Nanoclustering from Dimerization Indicates a Role for Clustering in CXCR4 Signaling and Function. *Mol Cell* **70**, 106-119.e10 (2018).

21. E. M. García-Cuesta, *et al.*, Altered CXCR4 dynamics at the cell membrane impairs directed cell migration in WHIM syndrome patients. *Proc Natl Acad Sci U S A* **119** (2022).

22. M. P. Wescott, *et al.*, Signal transmission through the CXC chemokine receptor 4 (CXCR4) transmembrane helices. *Proc Natl Acad Sci U S A* **113**, 9928–9933 (2016).

23. Q. Zhou, *et al.*, Common activation mechanism of class A GPCRs. *Elife* **8** (2019).

24. V. Sebastián-Pérez, *et al.*, Medicinal and Biological Chemistry (MBC) Library: An Efficient Source of New Hits. *J Chem Inf Model* **57**, 2143–2151 (2017).

25. A. Waterhouse, *et al.*, SWISS-MODEL: homology modelling of protein structures and complexes. *Nucleic Acids Res* **46**, W296–W303 (2018).

26. B. Haribabu, *et al.*, Regulation of human chemokine receptors CXCR4. Role of phosphorylation in desensitization and internalization. *J Biol Chem* **272**, 28726–28731 (1997).

27. R. Ameti, *et al.*, Characterization of a chimeric chemokine as a specific ligand for ACKR3. *J Leukoc Biol* **104**, 391–400 (2018).

28. R. K. Ganju, *et al.*, The alpha-chemokine, stromal cell-derived factor-1alpha, binds to the transmembrane G-protein-coupled CXCR-4 receptor and activates multiple signal transduction pathways. *J Biol Chem* **273**, 23169–23175 (1998).

29. S. R. Gardeta, *et al.*, Sphingomyelin Depletion Inhibits CXCR4 Dynamics and CXCL12-Mediated Directed Cell Migration in Human T Cells. *Front Immunol* **13** (2022).

30. K. W. Borrelli, A. Vitalis, R. Alcantara, V. Guallar, PELE: Protein Energy Landscape Exploration. A Novel Monte Carlo Based Technique. *J Chem Theory Comput* **1**, 1304–1311 (2005).

31. P. Rouhi, *et al.*, Hypoxia-induced metastasis model in embryonic zebrafish. *Nat Protoc* **5**, 1911–1918 (2010).

32. J. Xiao, E. Glasgow, S. Agarwal, Zebrafish Xenografts for Drug Discovery and Personalized Medicine. *Trends Cancer* **6**, 569–579 (2020).

33. H. K. Brown, K. Schiavone, S. Tazzyman, D. Heymann, T. J. A. Chico, Zebrafish xenograft models of cancer and metastasis for drug discovery. *Expert Opin Drug Discov* **12**, 379–389 (2017).

34. Y. You, *et al.*, Silibinin Induces G2/M Cell Cycle Arrest by Activating Drp1-Dependent Mitochondrial Fission in Cervical Cancer. *Front Pharmacol* **11** (2020).

35. T. Pozzobon, G. Goldoni, A. Viola, B. Molon, CXCR4 signaling in health and disease. *Immunol Lett* **177**, 6–15 (2016).

36. S. Fruehauf, W. J. Zeller, G. Calandra, Novel developments in stem cell mobilization: Focus on CXCR4. *Novel Developments in Stem Cell Mobilization: Focus on CXCR4*, 1–496 (2012).

37. H. Y. Choi, C. S. Yong, B. K. Yoo, Plerixafor for stem cell mobilization in patients with non-Hodgkin's lymphoma and multiple myeloma. *Ann Pharmacother* **44**, 117–126 (2010).

38. C. W. Hendrix, *et al.*, Safety, pharmacokinetics, and antiviral activity of AMD3100, a selective CXCR4 receptor inhibitor, in HIV-1 infection. *J Acquir Immune Defic Syndr* **37**, 1253–1262 (2004).

39. L. Martínez-Muñoz, B. L. Holgado, C. Martínez-A, J. M. Rodríguez-Frade, M. Mellado, Chemokine receptor oligomerization: a further step toward chemokine function. *Immunol Lett* **145**, 23–29 (2012).

40. A. Kumar, *et al.*, CXCR4 physically associates with the T cell receptor to signal in T cells. *Immunity* **25**, 213–224 (2006).

41. N. Ma, A. K. Nivedha, N. Vaidehi, Allosteric communication regulates ligand-specific GPCR activity. *FEBS J* **288**, 2502–2512 (2021).

42. G. Vauquelin, I. Van Liefde, G protein-coupled receptors: a count of 1001 conformations. *Fundam Clin Pharmacol* **19**, 45–56 (2005).

43. J. Wess, S. J. Han, S. K. Kim, K. A. Jacobson, J. H. Li, Conformational changes involved in G-protein-coupled-receptor activation. *Trends Pharmacol Sci* **29**, 616–625 (2008).

44. T. Kenakin, New concepts in pharmacological efficacy at 7TM receptors: IUPHAR review 2. *Br J Pharmacol* **168**, 554–575 (2013).

45. X. Yao, *et al.*, Coupling ligand structure to specific conformational switches in the beta2-adrenoceptor. *Nat Chem Biol* **2**, 417–422 (2006).

46. S. Chatterjee, B. Behnam Azad, S. Nimmagadda, The intricate role of CXCR4 in cancer. *Adv Cancer Res* **124**, 31–82 (2014).

47. K. Bourque, *et al.*, Distinct Conformational Dynamics of Three G Protein-Coupled Receptors Measured Using FlAsH-BRET Biosensors. *Front Endocrinol (Lausanne)* **8** (2017).

48. R. Nygaard, *et al.*, The dynamic process of β(2)-adrenergic receptor activation. *Cell* **152**, 532–542 (2013).

49. V. Sebastián-Pérez, *et al.*, Medicinal and Biological Chemistry (MBC) Library: An Efficient Source of New Hits. *J Chem Inf Model* **57**, 2143–2151 (2017).

50. B. Wu, *et al.*, Structures of the CXCR4 chemokine GPCR with small-molecule and cyclic peptide antagonists. *Science* **330**, 1066–1071 (2010).

51. G. Madhavi Sastry, M. Adzhigirey, T. Day, R. Annabhimoju, W. Sherman, Protein and ligand preparation: parameters, protocols, and influence on virtual screening enrichments. *J Comput Aided Mol Des* **27**, 221–234 (2013).

52. G. M. Morris, *et al.*, AutoDock4 and AutoDockTools4: Automated docking with selective receptor flexibility. *J Comput Chem* **30**, 2785–2791 (2009).

53. D. A. Case, *et al.*, Amber 14 (2014).

54. J. A. Maier, *et al.*, ff14SB: Improving the Accuracy of Protein Side Chain and Backbone Parameters from ff99SB. *J Chem Theory Comput* **11**, 3696–3713 (2015).

55. C. J. Dickson, *et al.*, Lipid14: The Amber Lipid Force Field. *J Chem Theory Comput* **10**, 865–879 (2014).

56. A. Vangone, A. Bonvin, PRODIGY: A Contact-based Predictor of Binding Affinity in Protein-protein Complexes. *Bio Protoc* **7** (2017).

57. K. Jaqaman, *et al.*, Robust single-particle tracking in live-cell time-lapse sequences. *Nat Methods* **5**, 695–702 (2008).

58. C. O. S. Sorzano, *et al.*, Image processing protocol for the analysis of the diffusion and cluster size of membrane receptors by fluorescence microscopy. *Journal of Visualized Experiments* **2019** (2019).

59. Y. R. Carrasco, S. J. Fleire, T. Cameron, M. L. Dustin, F. D. Batista, LFA-1/ICAM-1 interaction lowers the threshold of B cell activation by facilitating B cell adhesion and synapse formation. *Immunity* **20**, 589–599 (2004).

60. N. D. Lawson, B. M. Weinstein, In vivo imaging of embryonic vascular development using transgenic zebrafish. *Dev Biol* **248**, 307–318 (2002).

Figures and Tables

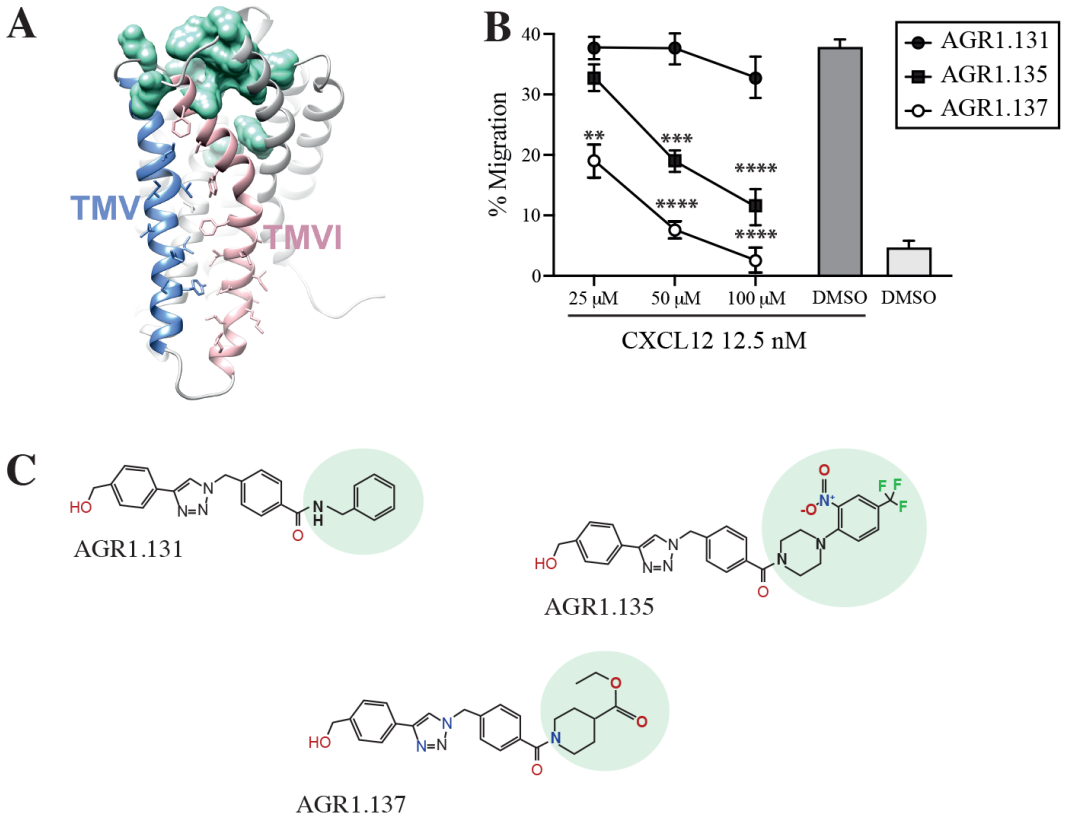

Figure 1. Screening for small compound antagonists acting on the oligomerization site of CXCR4. A) Surface representation of monomeric CXCR4 showing the cavity formed by TMV and TMVI. CXCR4 is shown in grey with TMV in blue and TMVI in pink. The cavity formed by both transmembrane helices includes some of the chemical chains of the participating residues. In green are shown the residues involved in CXCL12 binding. **B)** Dose-response curve of the selected antagonists in migration experiments of Jurkat cells in response to 12.5 nM CXCL12. Data are shown as percentage of migrating cells (mean ± SD; $n = 5$; ** ≤ 0.01, *** $p \leq 0.001$, **** $p \leq 0.0001$). **C)** Chemical structure of the selected compounds (AGR1.131, AGR1.135 and AGR1.137).

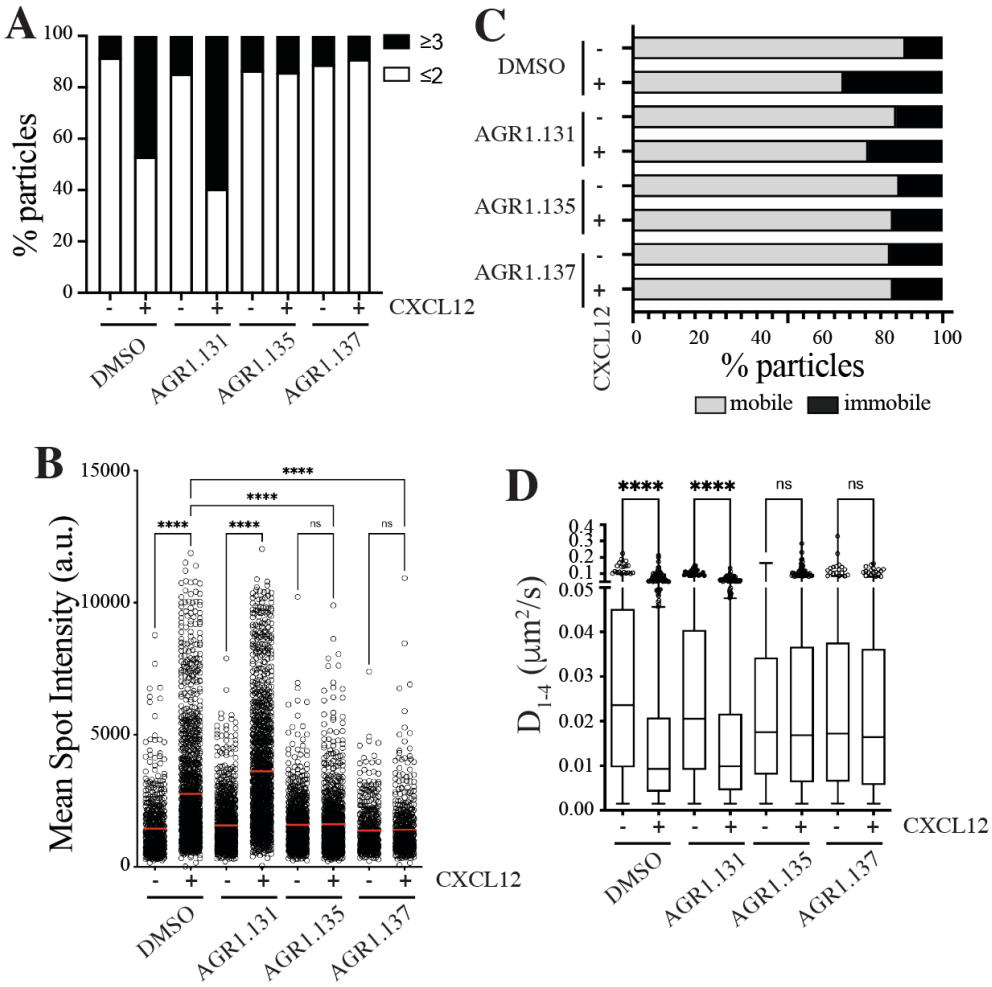

Figure 2. AGR1.135 and AGR1.137 alter CXCL12-mediated CXCR4 dynamics and nanoclustering. Single-particle tracking analysis of JK$^{-/-}$ transiently transfected with CXCR4 (JK$^{-/-}$-X4) cells treated with DMSO (control), AGR1.131, AGR1.135 or AGR1.137 on fibronectin (FN)- or FN+CXCL12-coated coverslips (DMSO: 581 particles in 59 cells on FN; 1365 in 63 cells on FN+CXCL12; AGR1.131: 1019 particles in 71 cells on FN; 1291 in 69 cells on FN+CXCL12; AGR1.135: 862 particles in 70 cells on FN; 1003 in 77 cells on FN+CXCL12; AGR1.137: 477 particles in 66 cells on FN; 566 in 64 cells on FN+CXCL12) n = 3. **A)** Frequency of CXCR4-AcGFP particles containing monomers plus dimers (≤2) or nanoclusters (≥3), calculated from mean spot intensity values of each particle as compared with the value of monomeric CD86-AcGFP. **B)** Intensity distribution (arbitrary units, a.u.) from individual CXCR4-AcGFP trajectories on unstimulated and CXCL12-stimulated JK$^{-/-}$-X4 cells pretreated or not with the indicated compounds, mean is indicated (red) (n = 3; n.s., not significant; ****p ≤ 0.0001). **C)** Percentage of mobile and immobile CXCR4-AcGFP particles at the membrane of cells as in (A) untreated or treated with the indicated compounds in basal conditions and after CXCL12 stimulation. **D)** Diffusion coefficients (D_{1-4}) of mobile single trajectories, with median (black line) corresponding to JK$^{-/-}$-X4 as in (a). (n.s., not significant, ****p ≤ 0.0001).

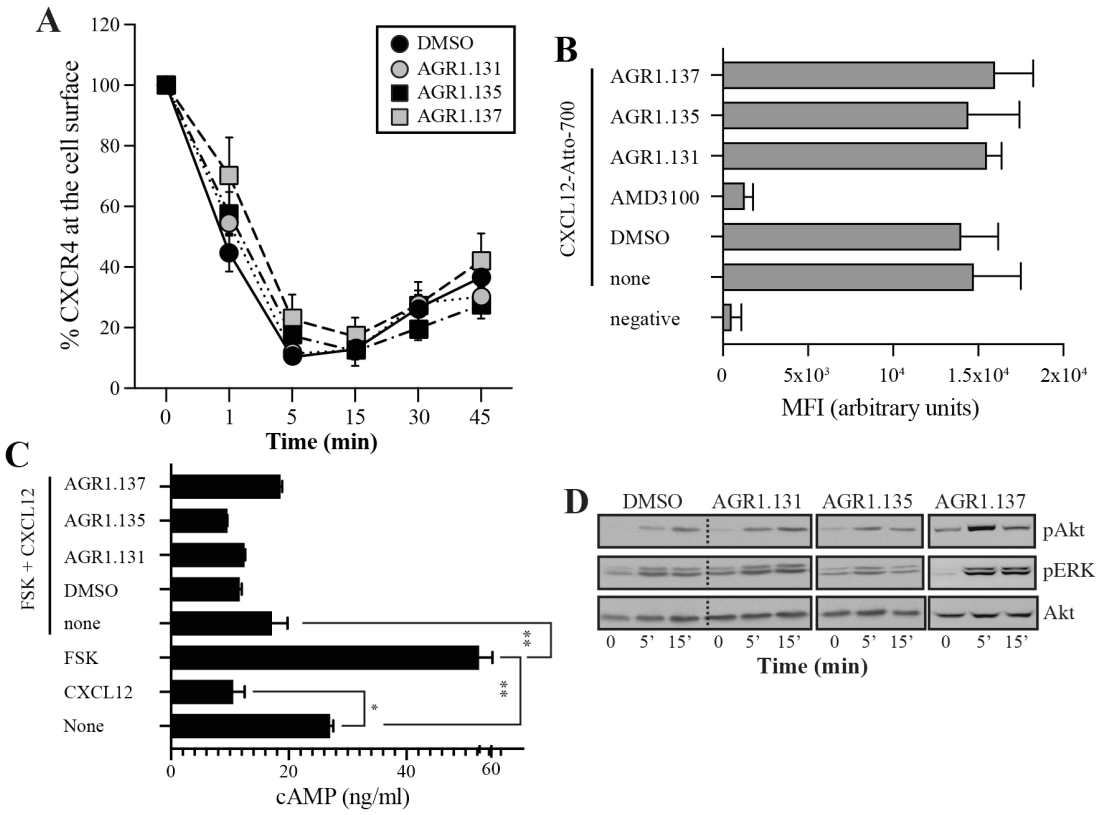

Figure 3. AGR1.135 and AGR1.137 treatments do not block CXCL12-mediated signaling pathways. A) Cell surface expression of CXCR4 in Jurkat cells after stimulation with CXCL12 (12.5 nM) at different time points and analyzed by flow cytometry using an anti-CXCR4 antibody in nonpermeabilized cells. Results show mean ± SEM of the percentage of CXCR4 expression at the cell surface (*n* = 4; n.s. not significant). **B)** CXCL12-Atto-700 binding on untreated or Jurkat cells pretreated with AGR1.131, AGR1.135 or AGR1.137 and with AMD-3100 as a control, followed by flow cytometry analysis. Results are expressed as mean fluorescence intensity (MFI) values (arbitrary units). Negative corresponds to basal cell fluorescence in the absence of CXCL12-Atto-700. **C)** Cells untreated or pretreated with the small compounds were stimulated with CXCL12 followed by forskolin. Cells were then lysed and cAMP levels were determined (mean ± SD; *n* = 3; n.s. not significant; *p ≤ 0.05, **p ≤ 0.01). **D)** Western blot analysis of phospho (p)Akt and pERK in Jurkat cells pre-treated with DMSO (vehicle), AGR1.131, AGR1.135 or AGR1.137, in response to CXCL12. As a loading control, membranes were re-blotted with an anti-Akt antibody. Representative experiments are shown (*n* = 4).

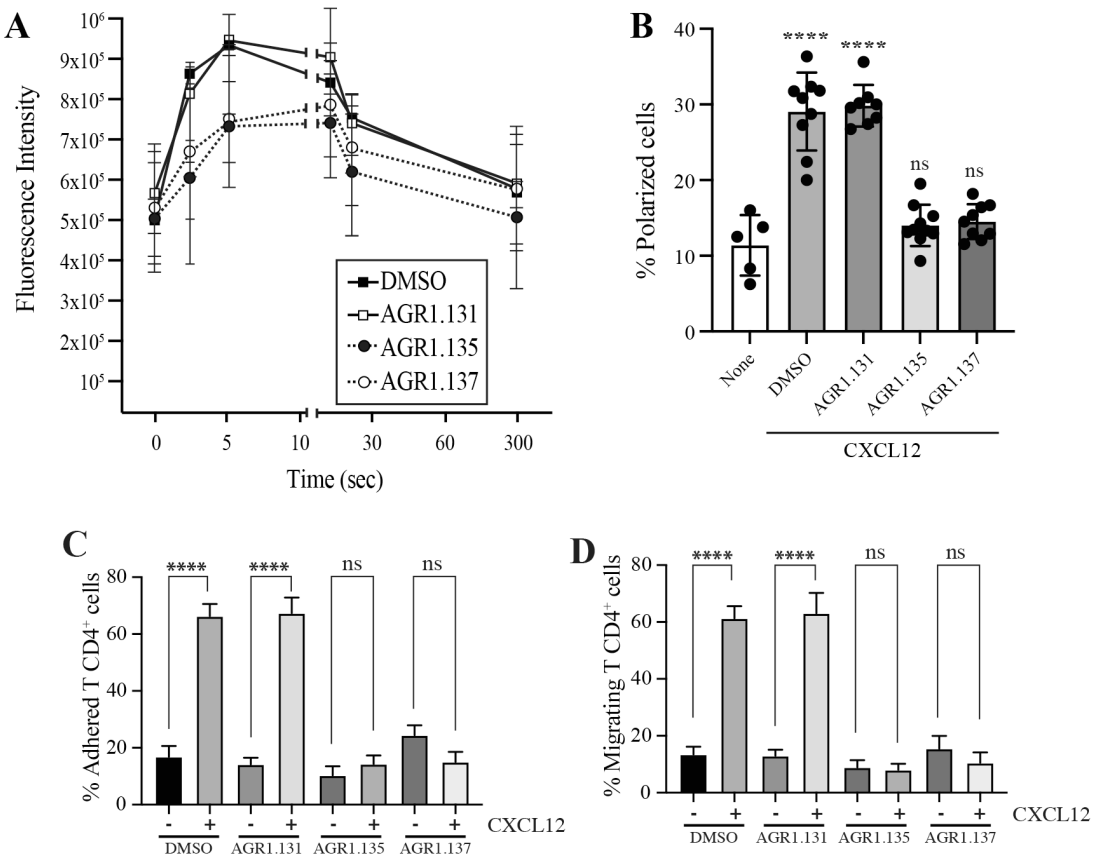

Figure 4. AGR1.135 and AGR1.137 treatment alter CXCL12-mediated actin polymerization. A) Actin polymerization in response to CXCL12 as determined by F-actin (phalloidin-TRITC) staining in JK cells untreated or treated with the indicated antagonists. B) Percentage of polarized T cell blasts adhered to fibronectin and treated or not with CXCL12 in the presence of the indicated antagonists, as analyzed by immunostaining with anti-ICAM3-Alexa fluor 488 and phalloidin-TRITC. More than 500 cell analyzed in each condition. Data are presented as percentage of polarized cells (mean +_SD; n=3; n.s. not significant; ****p< 0.0001). **C)** $CD4^+$ T cells pretreated with AGR1.131, AGR1.135 or AGR1.137 were perfused in flow chambers coated with ICAM-1 co-immobilized with CXCL12, and analyzed for cell contacts with the substrate. Data are presented as percentage of adhered cells (mean ± SD; *n* = 3; n.s. not significant; ****p ≤ 0.0001). **D)** Cells in (C) were analyzed for cell migration. Data are presented as percentage of migrating cells (mean ± SD; *n* = 3; n.s. not significant; ****p ≤ 0.0001).

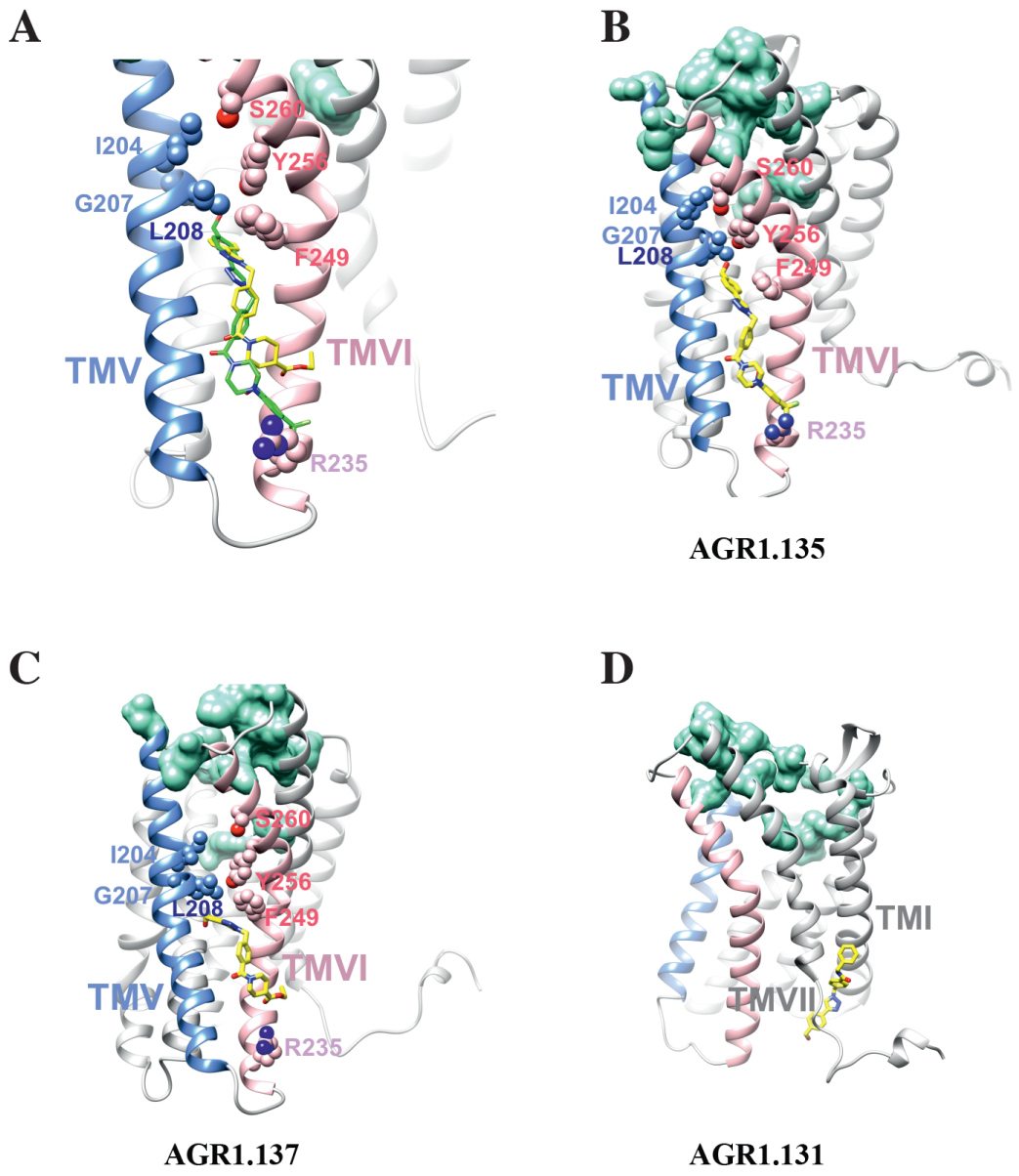

Figure 5. Ribbon and sticks representation of the CXCR4 modulators bound to the receptor. In the ribbon and sticks representations, TMV helix is colored in blue and TMVI in pink. Residues involved in CXCL12 engagement and initial signal transmission are represented in green and residues mutated are shown in spheres. **(A)** Superposition of AGR1.135 with carbons in green and AGR1.137 in yellow. **(B-D)** Show the binding of ligands AGR1.135 (B), AGR1.137 (C) and AGR1.131 (D) represented as sticks with carbon atoms in yellow, oxygens in red, nitrogens in blue and fluorines in green.

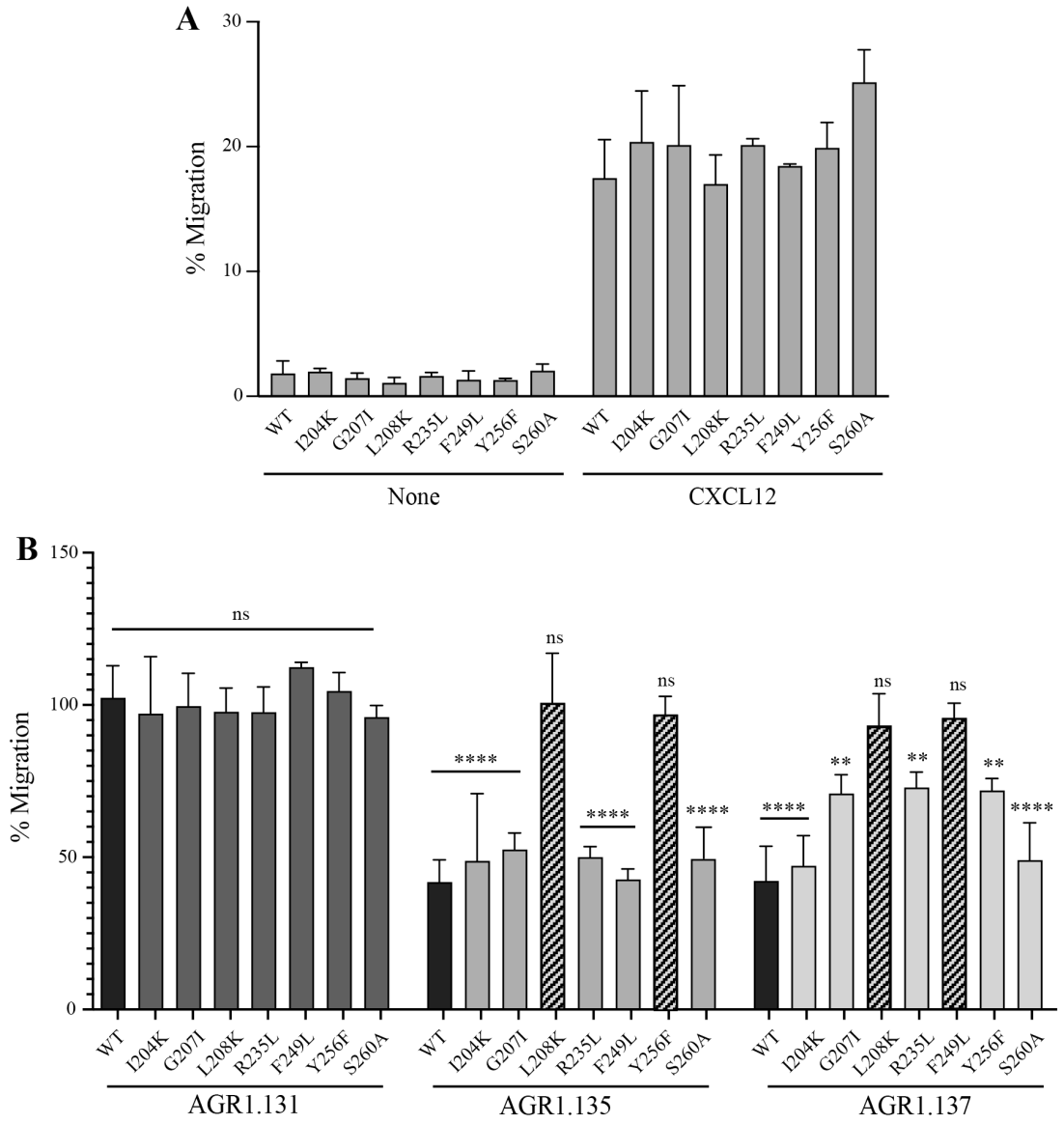

Figure 6. The antagonistic behavior of AGR1.135 and AGR1.137 depends on specific residues of CXCR4. A) CXCL12-induced migration of CXCR4-deficient Jurkat cells ($JK^{-/-}$) transiently transfected with CXCR4wt or its mutants, CXCR4I204K, CXCR4G207I, CXCR4L208K, CXCR4R235L, CXCR4F249L, CXCR4Y256F and CXCR4S260A. Data are shown as the mean percentage (plus SD) of input cells that migrate (*n* = 3). **B)** CXCL12-induced migration of AGR1.131- AGR1.135- or AGR1.137-pretreated $JK^{-/-}$ cells transiently transfected with CXCR4wt or the mutants described in (A). Data are shown as the mean percentage ± SD of input cells that migrate (*n* = 4; n.s. not significant, **p ≤ 0.01, ****p ≤ 0.0001).

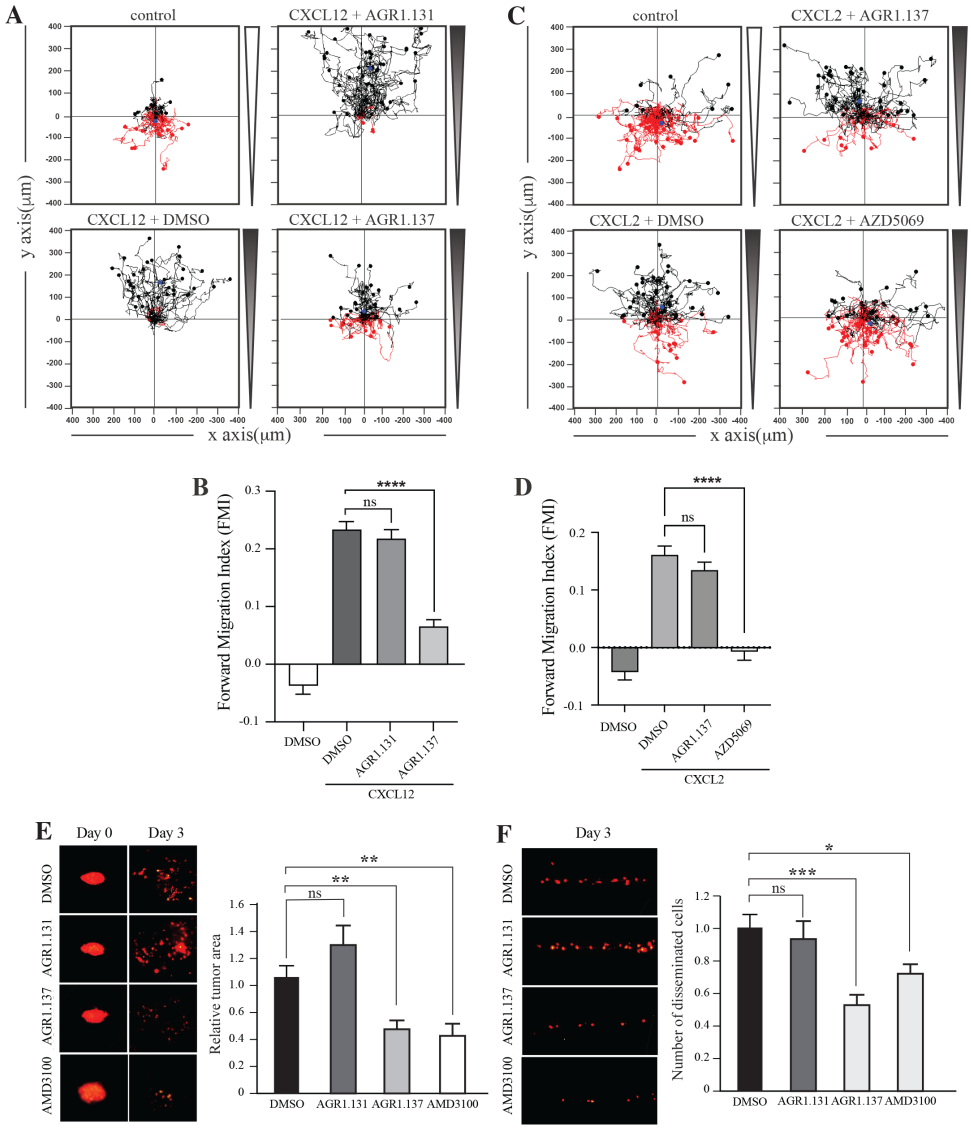

Figure 7. AGR1.137 reduces tumorigenesis and metastasis in a zebrafish model. A-D) Migration of HeLa cells treated with vehicle (DMSO) or with the selected small compounds or inhibitor as indicated, on µ-chambers in response to a CXCL12 (A,B) or CXCL2 (C,D) gradient (*n* = 2, in duplicate, with at least 50 cells tracked in each condition). Figures (A,C) shows representative spider plots with the trajectories of tracked cells migrating along the gradient (black) or moving in the opposite direction (red). Black and red dots in the plots represent the final position of each single tracked cell. B,D) Quantification of the Forward Migration Index of experiments performed in (A) and (C) (mean ± SD; *n* = 3; n.s. not significant, ****p ≤ 0.0001). **E)** Representative fluorescent images of DiI-labeled HeLa cells in zebrafish larvae treated with vehicle (DMSO), AGR1.131, AGR1.137 or AMD3100 at 0 or 3 days post-implantation and treatment. Quantitation of the relative tumor size at day 3 compared with that of day 0 is shown for each experimental group (mean ± SD; *n* = 20; n.s. not significant, **p ≤ 0.01). **F)** Representative fluorescent images of the caudal hematopoietic plexus of larvae from the same groups as shown in (E) at 3 days post-implantation. Quantitation of the average number of metastasized cells in each group (mean ± SD; *n* = 20, n.s. not significant, * p ≤ 0.05, *** p ≤ 0.001).

Supplementary Information for

Allosteric modulation of the CXCR4:CXCL12 axis by targeting receptor nanoclustering via the TMV-TMVI domain

Compound synthesis and characterization

1. General Experimental Details

2. Synthesis and Characterization of Triazol derivatives

3. NMR Spectra and HRMS Analysis

1. General Experimental Details

All solvents were purchased from Sigma-Aldrich (anhydrous solvents) and commercially available reagents were used as received. All reactions were followed by TLC analysis (TLC plates GF254, Merck) or LC–MS (liquid chromatography mass spectrometry). Melting points were determined in a Büchi Melting Point M-560 apparatus. NMR spectra were recorded at ambient temperature unless otherwise stated using standard pulse methods on any of the following spectrometers and signal frequencies: Bruker AV-300 (1H = 300 MHz, 13C = 75 MHz). Chemical shifts are reported in ppm and are referenced to tetramethylsilane (TMS) or to the following solvent peaks: CDCl3 (1H = 7.27 ppm, 13C = 77.00 ppm), DMSO-d6 (1H = 2.50 ppm, 13C = 39.51 ppm), Coupling constants are quoted to the nearest 0.1 Hz, and multiplicities are given by the following abbreviations and combinations thereof: s (singlet), d (doublet), t (triplet), q (quartet), m (multiplet), and br (broad). Column chromatography was performed on prepacked silica gel columns using a Biotage SP4 or Isolera One system. High resolution mass spectra (HRMS-ESI) were recorded on a Micromass Q-Tof Ultima hybrid quadrupole time-of-flight mass spectrometer, with analytes separated on an Agilent 1100 liquid chromatograph equipped with a Phenomenex Luna C18(2) reversed phase column (100 mm × 2.1 mm, 3 μm packing diameter).

2. Synthesis and Characterization of Triazol derivatives

General Procedure (GP):

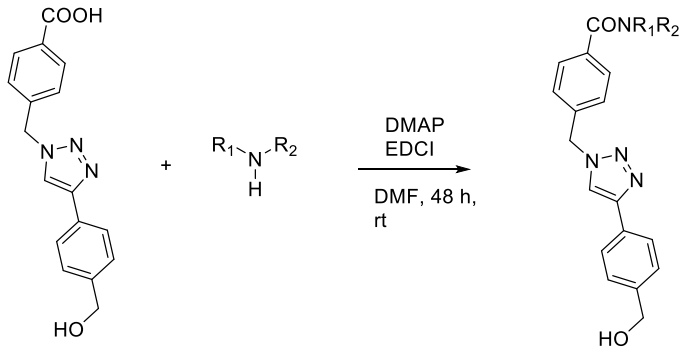

Over a solution of 4-((4-(4-(hydroxymethyl)phenyl)-1H-1,2,3-triazol-1-yl)methyl) benzoic acid (123 mg, 0.4 mmol) in 4 mL of DMF, DMAP (97 mg, 0.8 mmol) and EDC.HCl (92 mg, 0.48 mmol) were added and stirred for 15 min at room temperature. Subsequently, the corresponding amine (0.4 mmol) was added and stirred at room temperature for 48 h. Next, H_2O (10 ml) was added and extracted with DCM (25 ml × 3). The organic phase was dried over $MgSO_4$, filtered and evaporated under reduced pressure. The crude sample obtained was purified by column chromatography, eluting with DCM-MeOH solvent mixture (from 99:1 to 90:10).

_N_-Benzyl-4-((4-(4-(hydroxymethyl)phenyl)-1H-1,2,3-triazol-1-yl)methyl)benzamide (AGR1.131)

The reaction was performed according to GP using benzylamine (44 μl, 0.4 mmol), and the title product was obtained after purification by silica gel column chromatography as a white solid (35% yield). Pf: 193 – 195 ºC.

^{1}H NMR (300 MHz, DMSO-d_6) δ 9.09 (t, J = 6.0 Hz, 1H), 8.65 (s, 1H), 7.98 – 7.89 (m, 2H), 7.86 – 7.78 (m, 2H), 7.46 (d, J = 8.2 Hz, 2H), 7.40 (d, J = 8.1 Hz, 2H), 7.36 – 7.20 (m, 5H), 5.73 (s, 2H), 5.25 (t, J = 5.7 Hz, 1H), 4.53 (d, J = 5.7 Hz, 2H), 4.49 (d, J = 6.0 Hz, 2H). ^{13}C NMR (75 MHz, DMSO) δ 165.69, 146.69, 142.29, 139.56, 139.01, 134.08, 128.99, 128.25, 127.83, 127.74, 127.12, 126.88, 126.71, 124.90, 121.42, 62.61, 52.58, 42.56.
HRMS (ESI$^+$) m/z Calc. Para $C_{24}H_{23}N_4O_2$ [M+H] $^+$: 399.1816. Found: 399.1809.

(4-((4-(4-(Hydroxymethyl)phenyl)-1H-1,2,3-triazol-1-yl)methyl)phenyl)(4-(2-nitro-4-(trifluoromethyl)phenyl)piperazin-1-yl)methanone (AGR1.135)

The reaction was performed according to GP using (2-nitro-4-(trifluoromethyl)phenyl)piperazine (110 mg, 0.4 mmol), and the title product was obtained after purification by silica gel column chromatography as a yellow solid (37% yield). Pf: 184 – 186 ºC.

^{1}H NMR (300 MHz, DMSO-d_6) δ 8.65 (s, 1H), 8.19 (d, J = 2.3 Hz, 1H), 7.89 (dd, J = 8.9, 2.3 Hz, 1H), 7.81 (d, J = 8.0 Hz, 2H), 7.53 – 7.35 (m, 7H), 5.71 (s, 2H), 5.23 (t, J = 5.7 Hz, 1H), 4.52 (d, J = 5.4 Hz, 2H), 3.73 (s, 2H), 3.48 (s, 2H), 3.21 (s, 4H). ^{13}C NMR (75 MHz, DMSO) δ 169.12, 147.70, 147.08, 142.67, 140.04, 137.84, 135.74, 130.59, 130.54, 129.38, 128.27, 128.00, 127.25, 125.65, 125.29, 124.12, 124.07, 122.06, 121.92, 121.82, 120.57, 120.12, 62.99, 62.87, 52.97, 50.33, 47.01.
HRMS (ESI$^+$) Calc. para $C_{28}H_{26}F_3N_6O_4$ [M+H] $^+$: 567.1962. Found: 567.1959.

Ethyl 1-(4-((4-(4-(hydroxymethyl)phenyl)-1H-1,2,3-triazol-1-yl)methyl)benzoyl) piperidine-4-carboxylate (AGR1.137)

The reaction was performed according to GP using ethyl piperidinee-4-carboxylate (63 mg, 0.4 mmol) and the title product was obtained after purification by silica gel column chromatography as a white solid (30% yield). Pf: 119 – 121 ºC.

^{1}H NMR (300 MHz, Methanol-d_4) δ 8.40 (s, 1H), 7.89 – 7.74 (m, 2H), 7.56 – 7.31 (m, 6H), 5.73 (s, 2H), 4.66 (s, 2H), 4.48 (d, J = 13.2 Hz, 1H), 4.16 (q, J = 7.1 Hz, 2H), 3.69 (d, J = 13.0 Hz, 1H), 3.24 – 2.96 (m, 2H), 2.78 – 2.52 (m, 1H), 2.15 – 1.52 (m, 4H), 1.27 (t, J = 7.1 Hz, 3H). ^{13}C NMR (75 MHz, MeOD) δ 175.82, 171.87, 149.21, 143.15, 138.81,

137.25, 130.56, 129.43, 128.59, 128.56, 126.71, 122.39, 64.88, 61.79, 54.58, 42.65, 41.96, 29.67, 28.96, 14.51.
HRMS (ESI$^+$) Calc. para $C_{25}H_{29}N_4O_4$ $[M+H]^+$: 449.2183. Found: 449.2160.

3. NMR Spectra and HRMS Analysis

(AGR1.131)

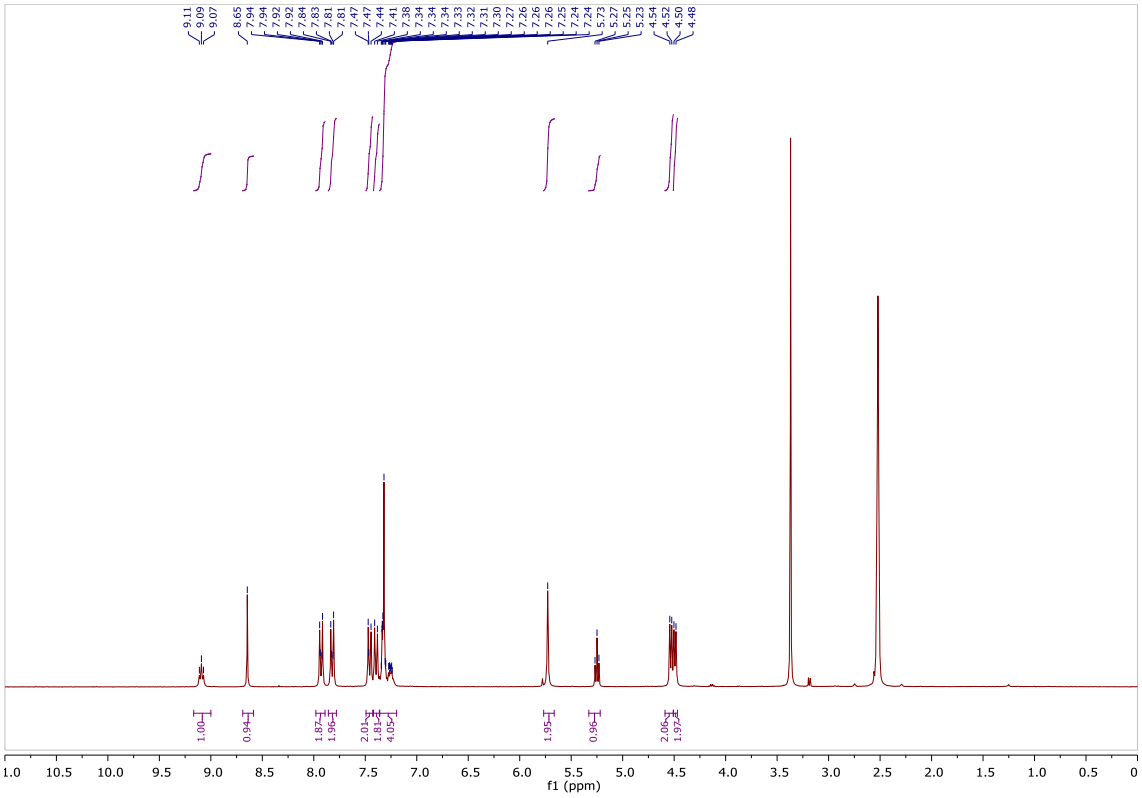

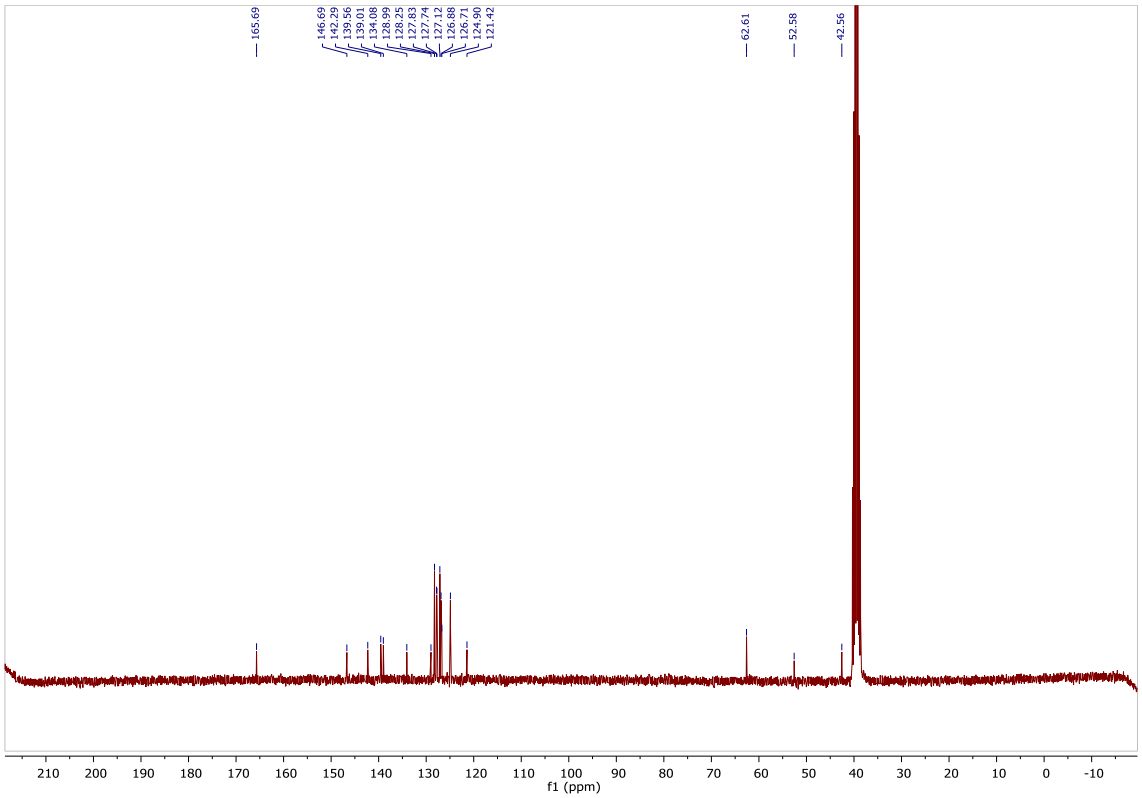

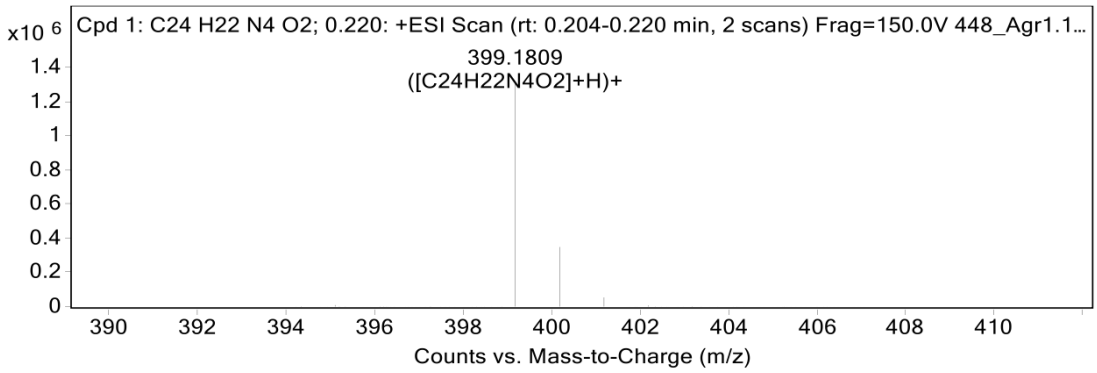
Cpd 1: C24 H22 N4 O2; 0.220: +ESI Scan (rt: 0.204-0.220 min, 2 scans) Frag=150.0V 448_Agr1.1...
x10 6
399.1809
([C24H22N4O2]+H)+
1.4
1.2
1
0.8
0.6
0.4
0.2
0
390
392
394
396
398
400
402
404
406
408
410
Counts vs. Mass-to-Charge (m/z)

(AGR1.135)

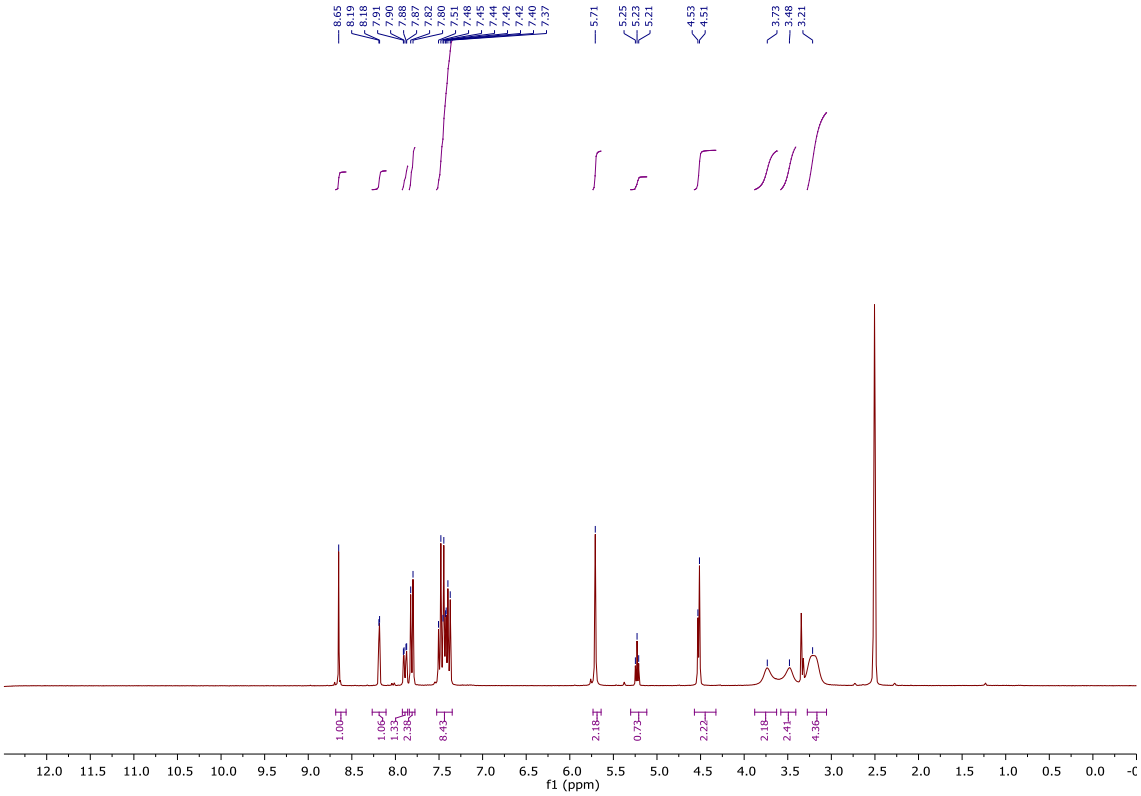
8.65
8.19
8.18
7.91
7.90
7.88
7.87
7.82
7.80
7.51
7.48
7.45
7.44
7.42
7.42
7.40
7.37
5.71
5.25
5.23
5.21
4.53
4.51
3.73
3.48
3.21
1.00
1.06
1.33
2.38
8.43
2.18
0.73
2.22
2.18
2.41
4.36
f1 (ppm)

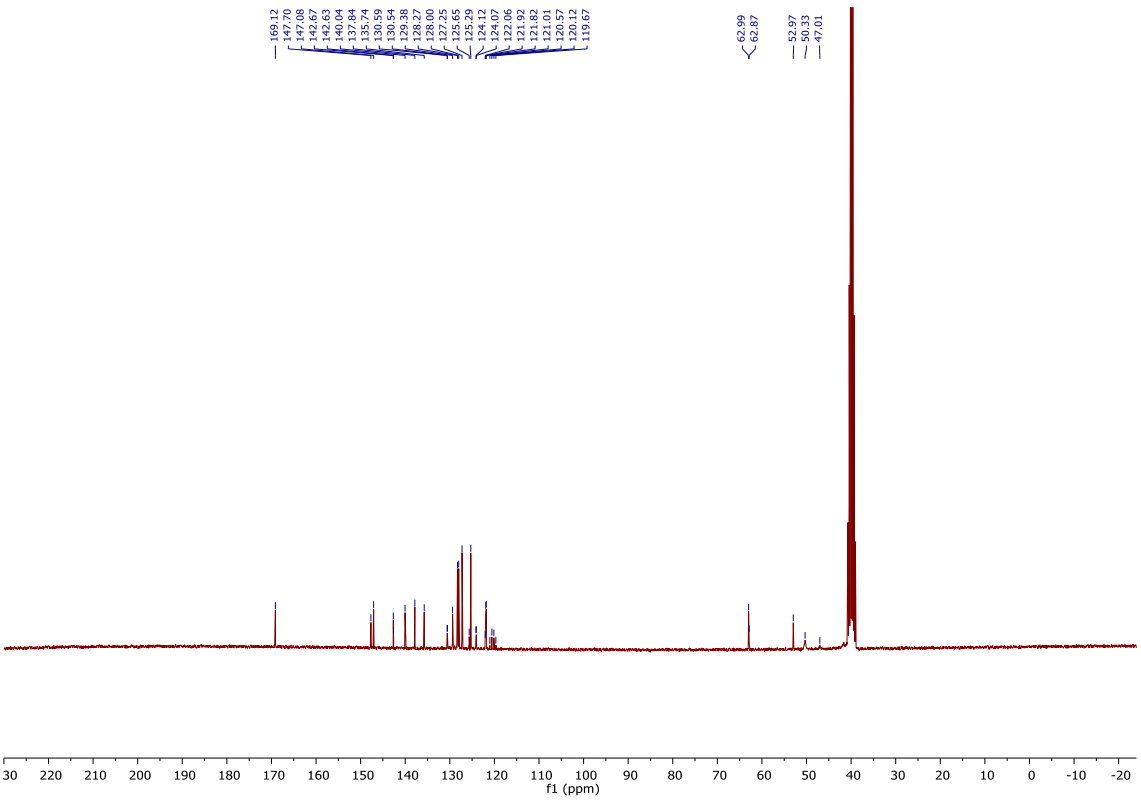
169.12
147.70
147.08
142.67
142.63
140.04
137.84
135.74
130.59
130.54
129.38
128.27
128.00
127.25
125.65
125.29
124.12
124.07
122.06
121.92
121.82
121.01
120.57
120.12
119.67
62.99
62.87
52.97
50.33
47.01
f1 (ppm)

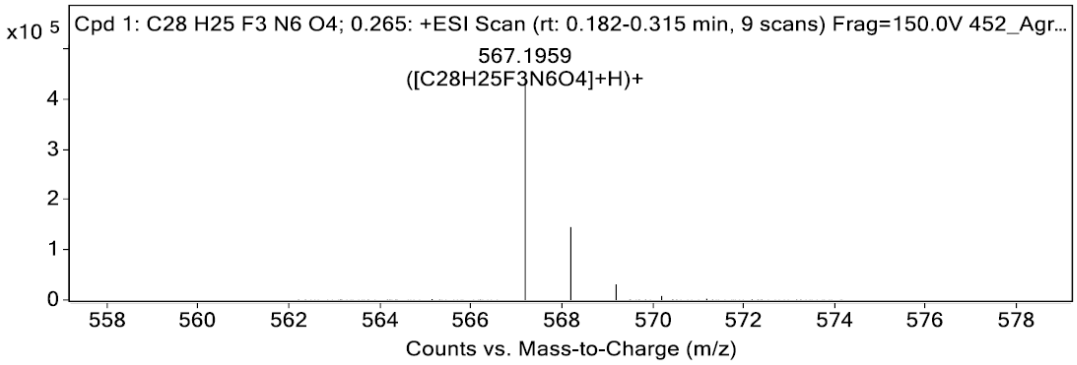
Cpd 1: C28 H25 F3 N6 O4; 0.265: +ESI Scan (rt: 0.182-0.315 min, 9 scans) Frag=150.0V 452_Agr...
x10 5
567.1959
([C28H25F3N6O4]+H)+
Counts vs. Mass-to-Charge (m/z)

(AGR1.137)

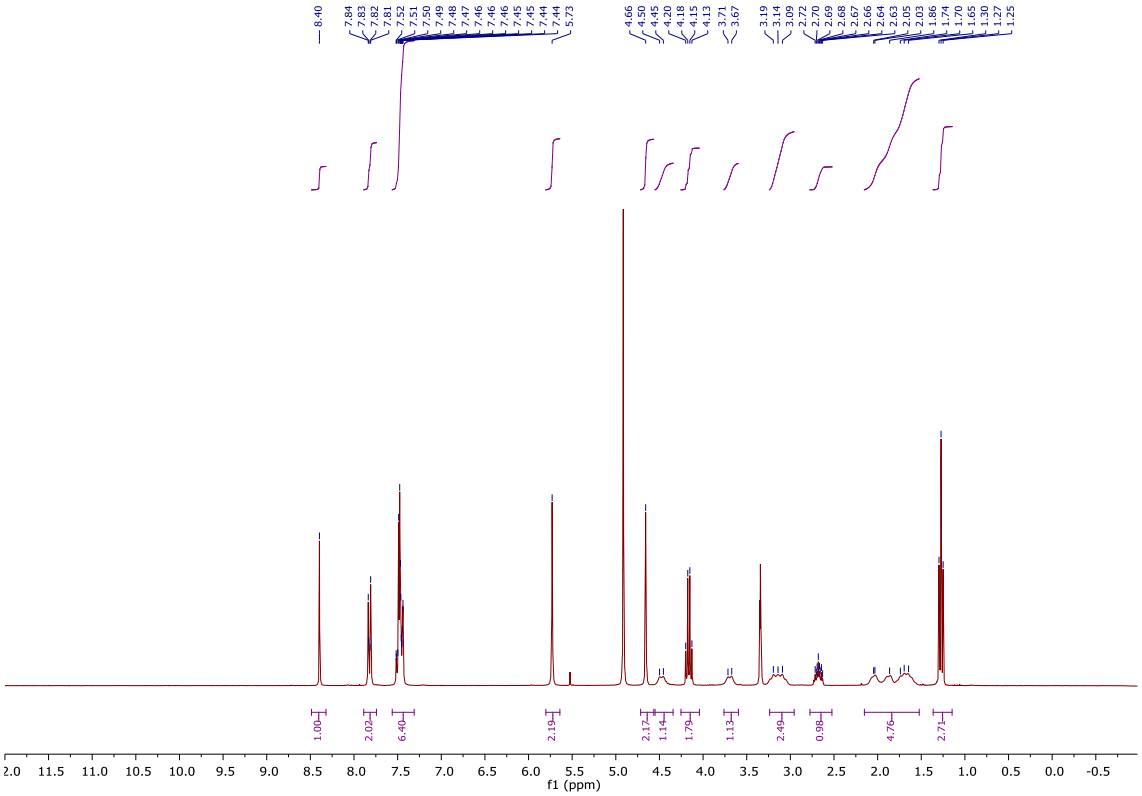
f1 (ppm)

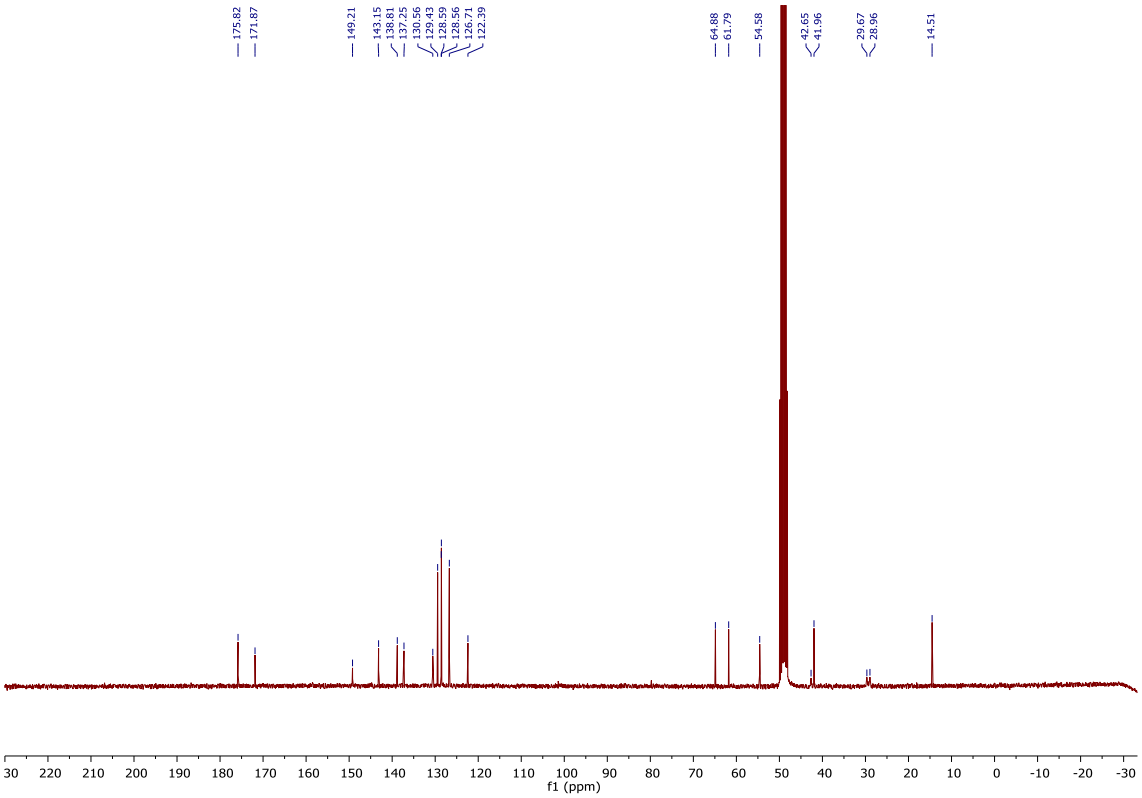
175.82
171.87
149.21
143.15
138.81
137.25
130.56
129.43
128.59
128.56
126.71
122.39
64.88
61.79
54.58
42.65
41.96
29.67
28.96
14.51
f1 (ppm)

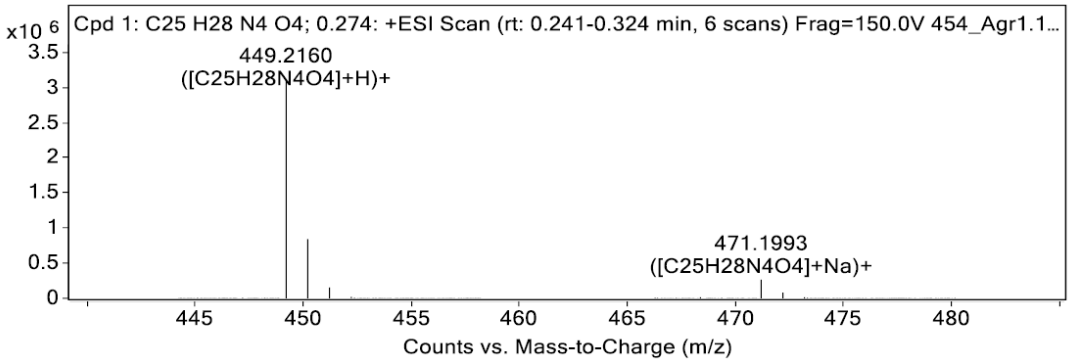
Cpd 1: C25 H28 N4 O4; 0.274: +ESI Scan (rt: 0.241-0.324 min, 6 scans) Frag=150.0V 454_Agr1.1...
x10 6
449.2160
([C25H28N4O4]+H)+
471.1993
([C25H28N4O4]+Na)+
Counts vs. Mass-to-Charge (m/z)

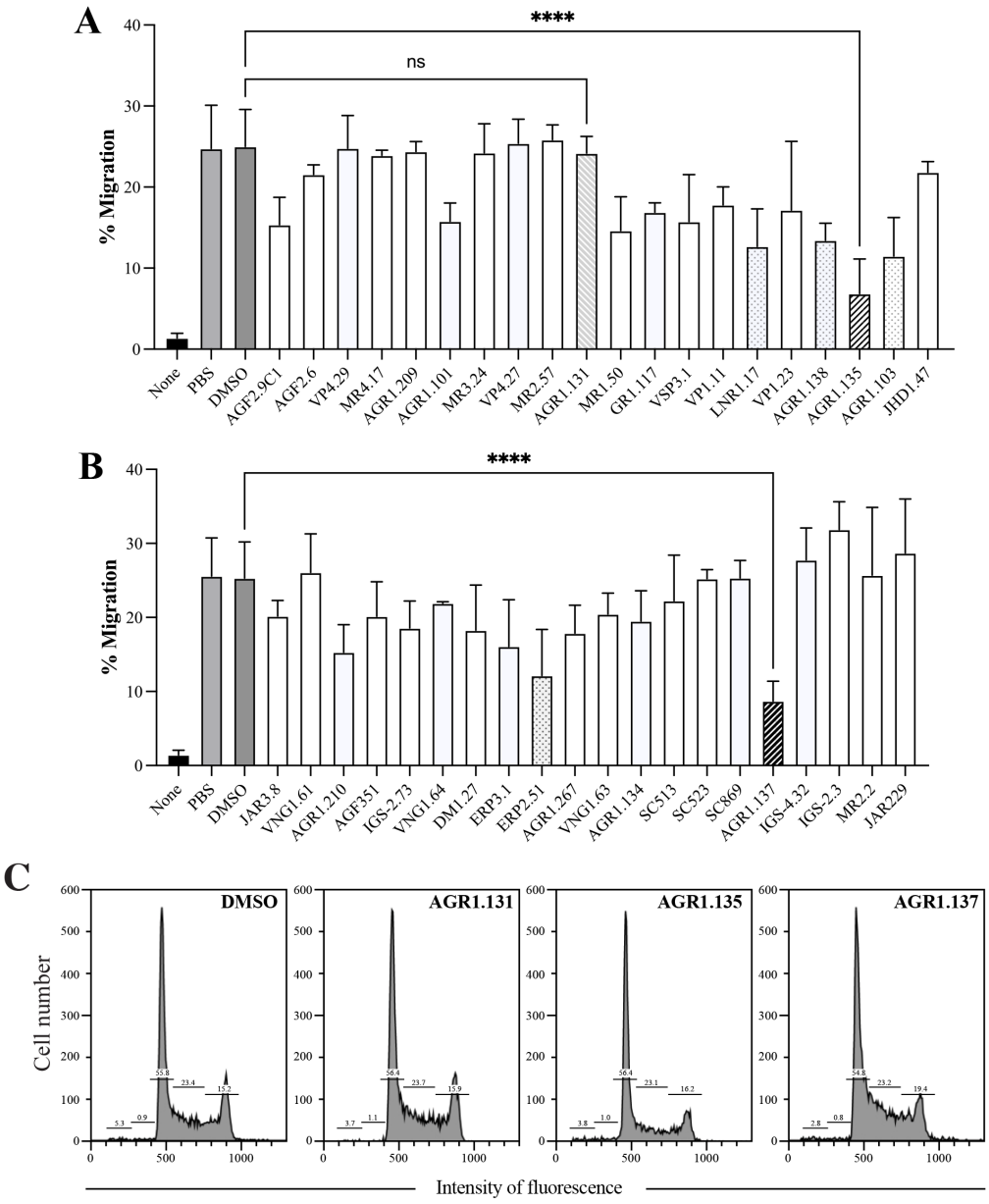

Supplementary Figure 1. Small compound-mediated inhibition of CXCL-12-induced cell migration. A, B) Migration of Jurkat cells, untreated or treated with the selected small compounds (50 μM) in the *in silico* screening, in response to 12.5 nM CXCL12. Data shown as percentage of migrating cells (mean ± SD; n = 5; **** p ≤0.0001, ns : not significant). **C)** Cell cycle analysis using propidium iodide incorporation and flow cytometry of Jurkat cells treated with AGR1.131, AGR1.135 and AGR1.137 (2 hours, 37ºC) or with DMSO as control. The percentage of cells in each cycle stage is shown.

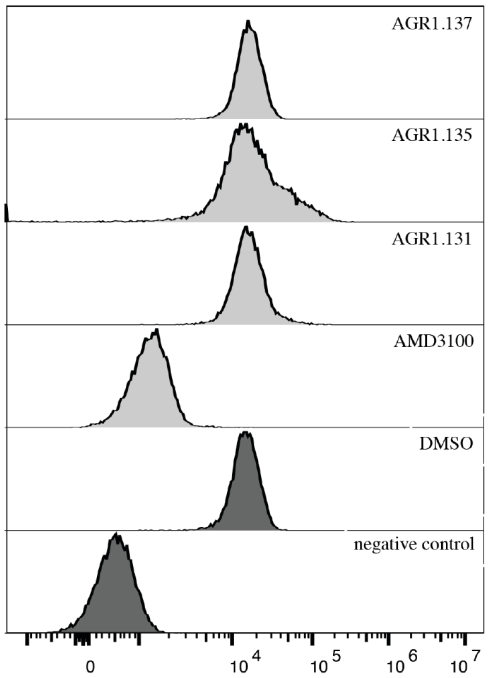

Supplementary Figure 2. Flow cytometry analysis of the binding of CXCL12-ATTO700 to JK cells. Cells were pre-incubated for 30 min at 37ºC with the indicated antagonists, followed by incubation with CXCL12- ATTO700 (30 min 37ºC). CXCL12 binding was determined in flow cytometry. A representative experiment of 4 performed is shown.

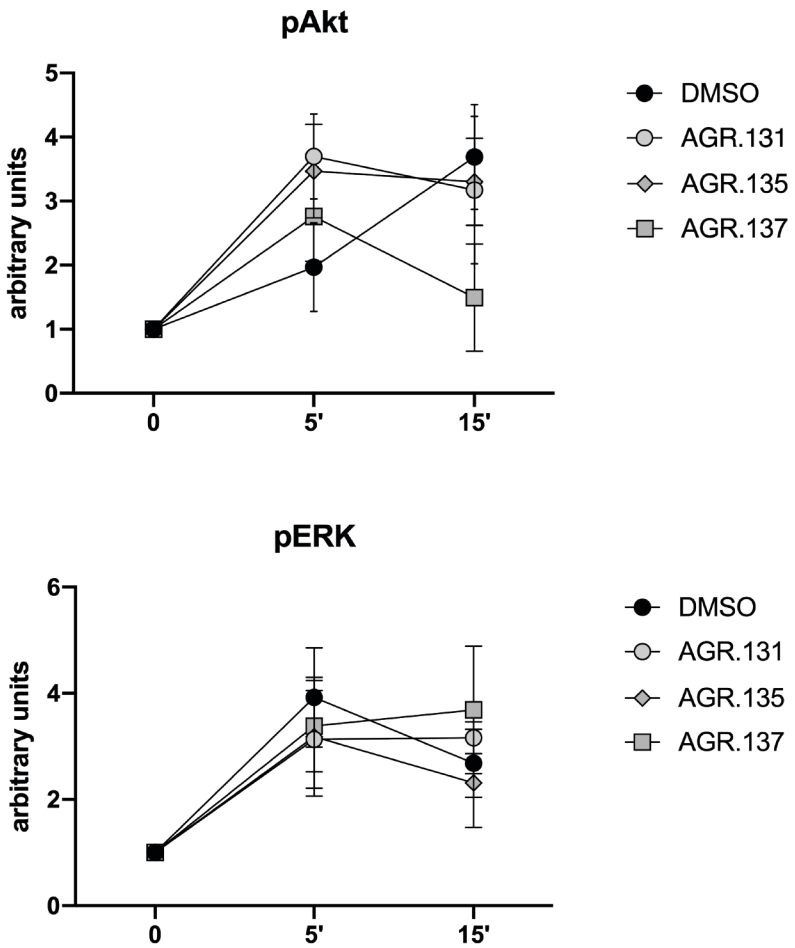

Supplementary Figure 3. Densitometry evaluation of the western blot experiments. Western blot analysis of pAkt and P-ERK in Jurkat cells pre-treated with AGR1.131, AGR1.135 and AGR1.137 in response to CXCL12 were performed (Figure 3B). The figure shows the densitometry evaluation of the specific bands (mean ± SD; n = 4).

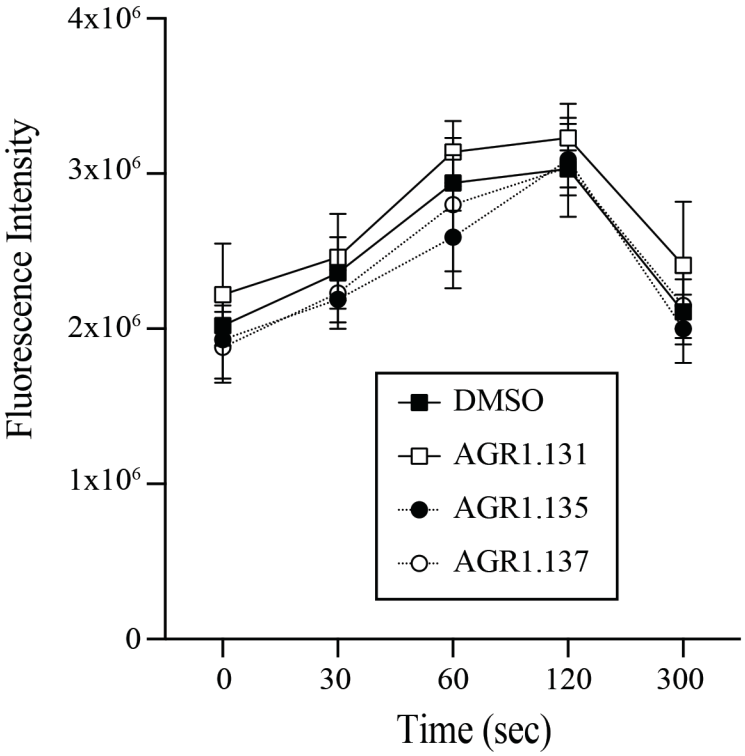

Supplementary Figure 4. AGR1.135 and AGR1.137 do not alter anti-CD3-induced actin polimerization. F-actin (Phalloidin-TRITC) staining of Jurkat cells untreated or treated with the indicaed antagonists, adhered to fibronectin and treated with anti-CD3 antibody, as indicated (mean ± SD; n = 3).

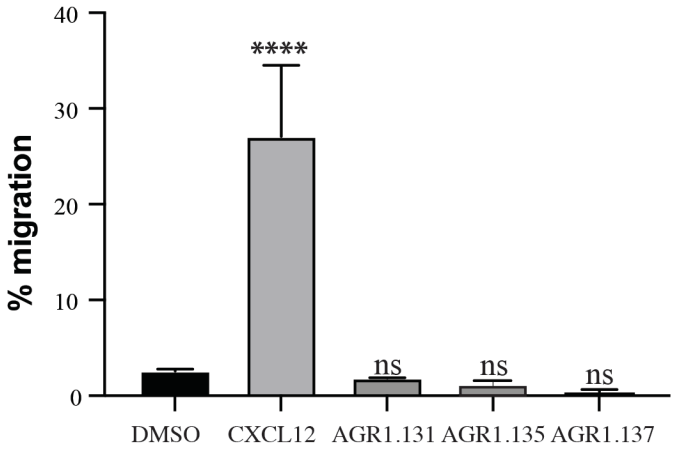

Supplementary Figure 5. AGR1.131, AGR1.135 and AGR1.137 are not CXCR4 agonists. Migration of Jurkat cells in response to 12.5 nM CXCL12, 50 μM AGR1.131, 50 μM AGR1.135 or 50 μM AGR1.137. Data shown as percentage of migrating cells (mean ± SD; n = 5; n.s. not significant, **** $p \leq 0.0001$).

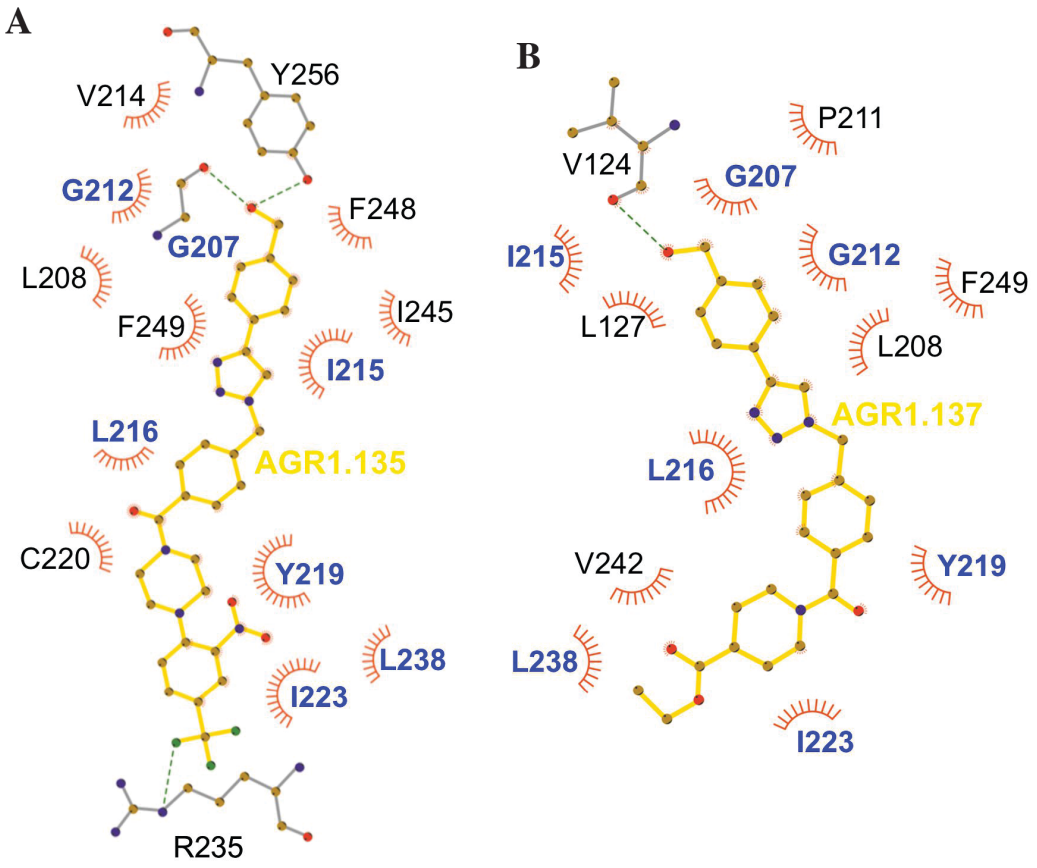

Supplementary Figure 6. Ligplot representation of antagonists interactions with CXCR4. Ligplot representations of AGR1.135 (**A**) and AGR1.137 (**B**), with hydrogen bonds represented in green dotted lines and non-bonded contacts in red spoke arcs. Residues labeled in blue font are present in the interface of both AGR1.135 and AGR1.137. CXCR4 residues forming a hydrogen bond with the ligands are shown in gray.

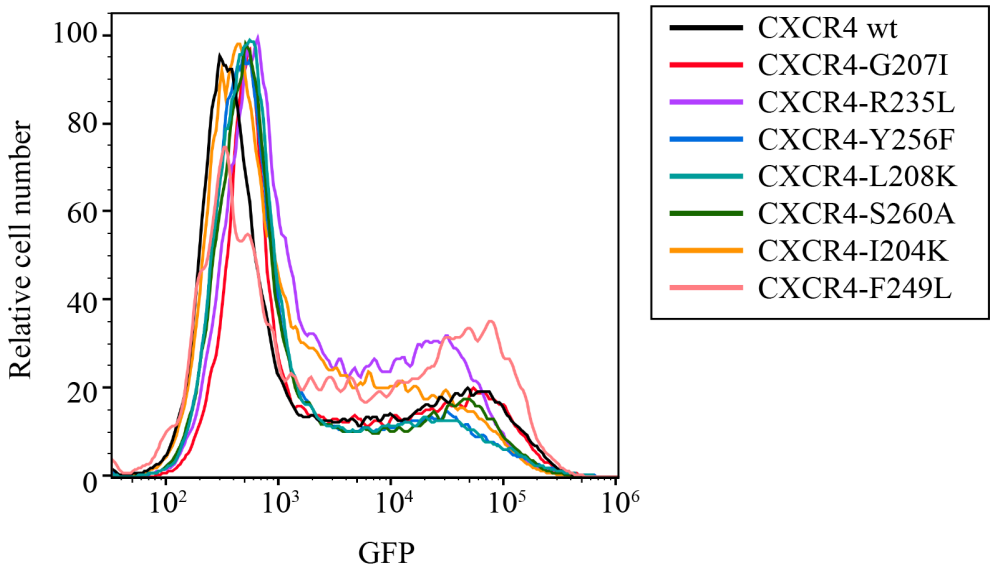

Supplementary Figure 7. Flow cytometry analysis of the expression of CXCR4 and CXCR4 mutants coupled to AcGFP in transfected JK$^{-/-}$ cells. Cells were transiently transfected with the indicated CXCR4 mutants or wt CXCR4, coupled to AcGFP and their expression was determined 24 hours after transfection by GFP detection in flow cytometry. A representative experiment of 4 performed is shown.

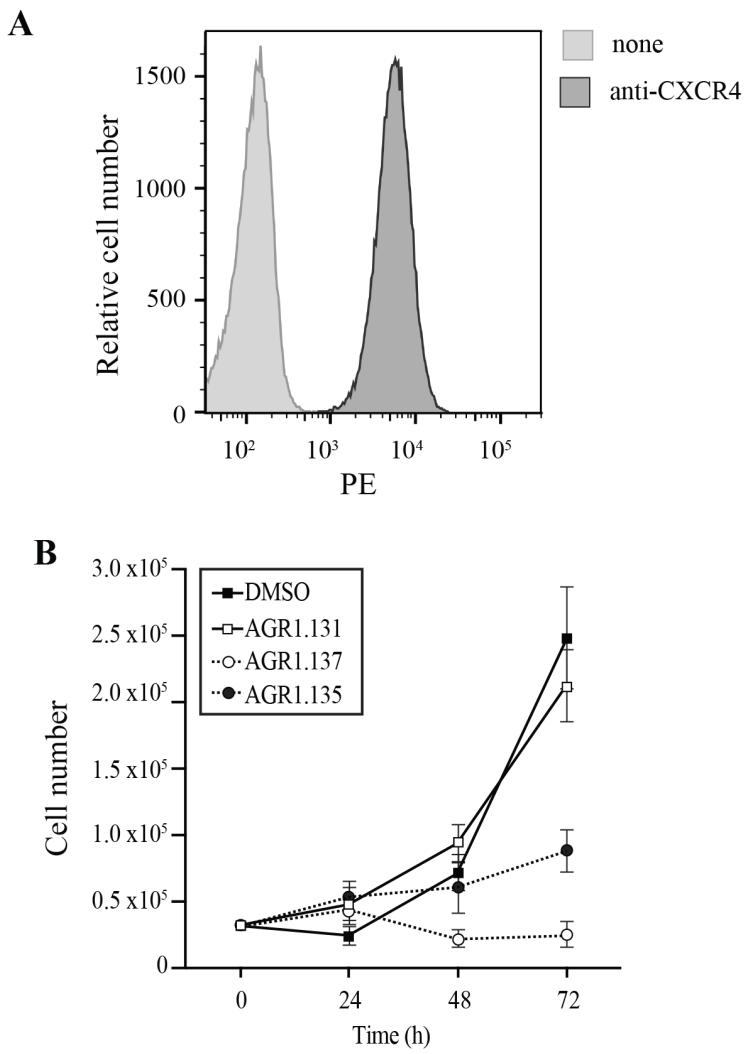

Supplementary Figure 8. Characterization of HeLa cells. A) CXCR4 expression on the surface of HeLa cells, analyzed by flow cytometry using a specific antibody. Data show a representative experiment of 6 performed. **B**) Effect of the indicated compounds on HeLa cells growth. Cells ($0.5x10^6$) were plated on 48 well plates in the presence of 100 μM of the compounds, which were added freshly every 24 hours. Cells were counted at every 24 hours and maintained for 72 h. The mean of three different experiments is shown.

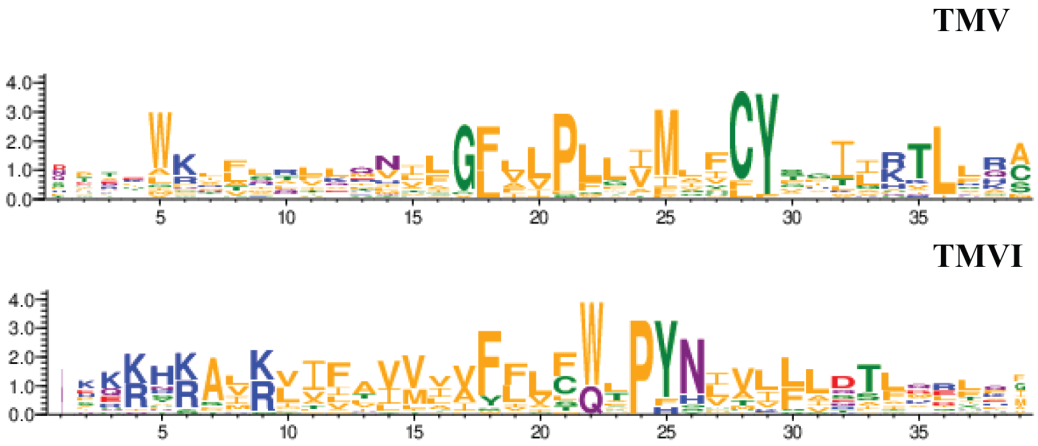

Supplementary Figure 9. Residue conservation among all GPCR class A chemokine receptors for TMV and TMVI. Graphs were produced in the WebLogo server after aligning all receptors sequence in the sequence alignment tool included in GPCRdb. Font size for each residue represented in one letter code stands for the degree of conservation among all chemokine receptors. Residues are colored by their chemistry being green for polar, orange for hydrophobic, red for acidic, blue for basic and purple for neutral.

Supplementary Table 1. Compounds with minimal interaction energy in the area of interest

Ref.	Structure	Ref.	Structure
#1 AGF2.9 C1	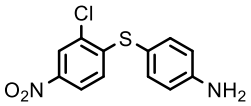	#15 LNR1.17	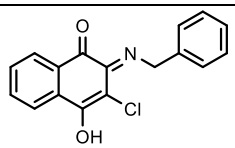
#2 AGF2.6	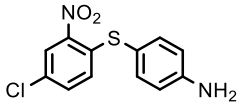	#16 VP1.23	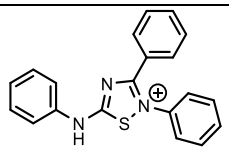
#3 VP4.29	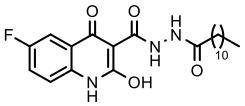	#17 AGR1.138	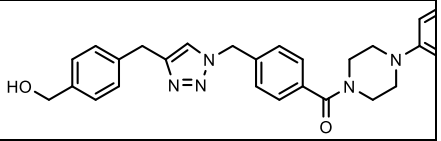
#4 MR4.17	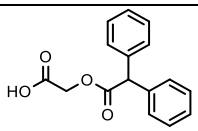	#18 AGR1.103	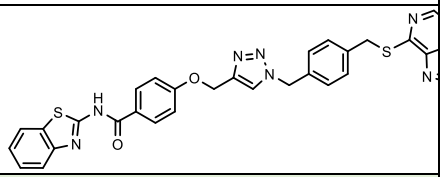
#5 AGR1.209	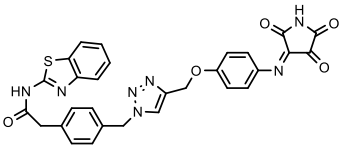	#19 AGR1.135	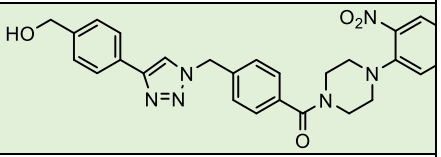
#6 AGR1.101	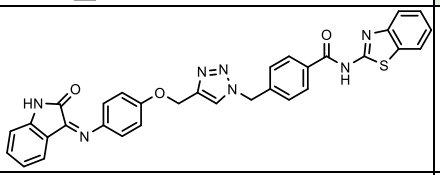	#20 JHD1.47	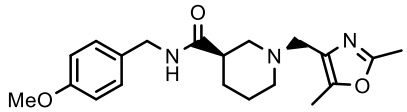
#7 MR3.24	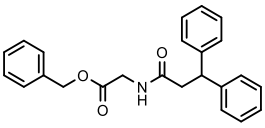	#21 JAR3.8	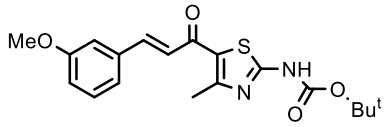
#8 VP4.27	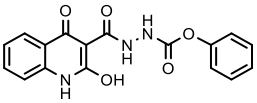	#22 VNG1.61	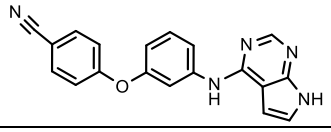
#9 MR2.57	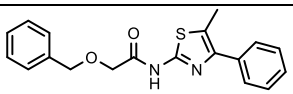	#23 AGR1.210	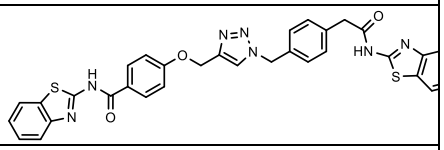
#10 AGR1.131	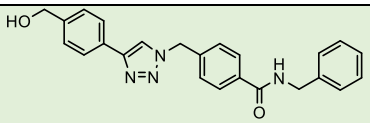	#24 AGF351	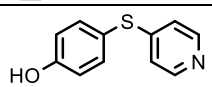
#11 MR1.50	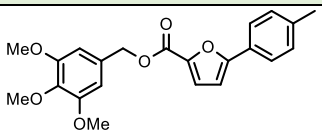	#25 IGS-2.73	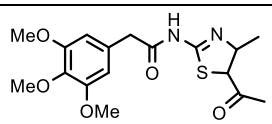
#12 AGR1.117	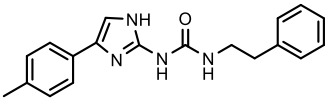	#26 VNG1.64	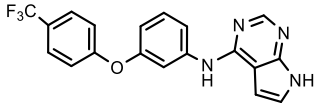

#13 VSP3.1	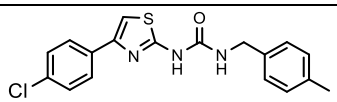	#27 DM1.27	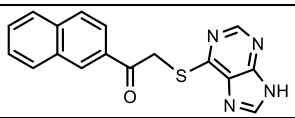
#14 VP1.11	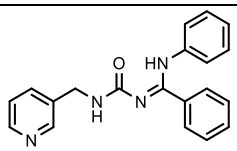	#28 ERP3.1	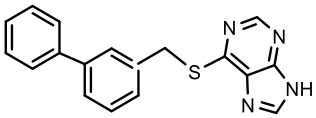
Ref.	Structure	Ref.	Structure
#29 ERP2.51	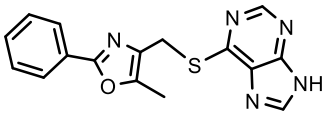	#35 SC089	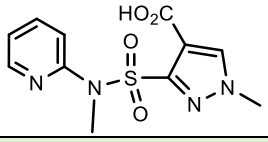
#30 AGR1.2 67	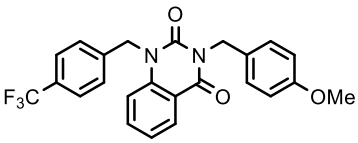	#36 AGR1.1 37	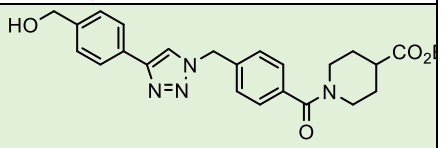
#31 VNG1.3 6	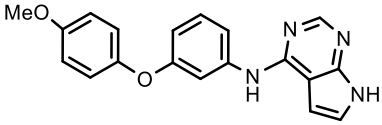	#37 IGS- 4.32	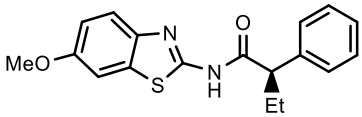
#32 AGR1.1 34	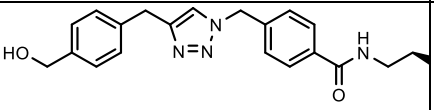	#38 IGS-2.3	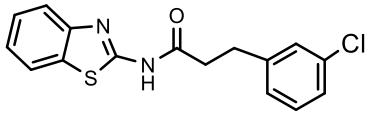
#33 SC513	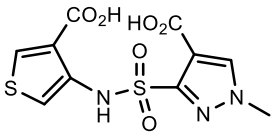	#39 MR2.2	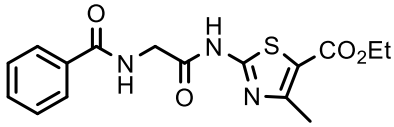
#34 SC523	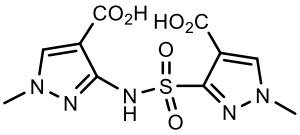	#40 JAR229	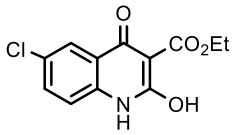

Structure of the compounds employed in the study. Highlighted in green boxes are shown the compounds studied in detail (AGR1.131, AGR1.135 and AGR1.137).

Supplementary Table S. Oligonucleotides used to generate the CXCR4 mutants

Mutation	Forward	Reverse
CXCR4 G207I	CAC ATC ATG GTT ATT CTT ATC CTG CCT	AGG CAG GAT AAG AAT AAC CAT GAT GTG
CXCR4 R235L	GGC CAC CAG AAG TTA AAG GCC CTC AAG	CTT GAG GGC CTT TAA CTT CTG GTG GCC
CXCR4 Y256F	TGG CTG CCT TAC TTT ATT GGG ATC AGC	GCT GAT CCC AAT AAA GTA AGG CAG CCA
CXCR4 S260A	TACTACATTGGGATCGCCATCGACTCCTTCATC	GATGAAGGAGTCGATGGCGATCCCAATGTAGTA
CXCR4 L208K	CACATCATGGTTGGCAAGATCCTGCCTGGTATT	AATACCAGGCAGGATCTTGCCAACCATGATGTG
CXCR4 I204K	TTCCAGTTTCAGCACAAGATGGTTGGCCTTATC	GATAAGGCCAACCATCTTGTGCTGAAACTGGAA
CXCR4 G212F	GCCCTTATCCTGCCTTTCATTGTCATCCTGTCC	GGACAGGATGACAATGAAAGGCAGGATAAGGCC
CXCR4 F249L	GTCATCCTCATCCTGGCTTTCTGCCTGTTGGCT GCCT	AGGCAGCCAACAGGCCAGGAAAGCCAGGATGAGGA TGAC

Movie S1 (separate file). Related to Figure 6A. Representative video of DMSO-treated HeLa cell migration on fibronectin-coated μ-Slide Chemotaxis chambers in the absence of CXCL12 gradient. Images over time (15 frames/s) are shown. Overlaid trajectories of cells shown in movie were detected and tracked using Fiji software.

Movie S2(separate file)

Related to Figure 6A. Representative video of DMSO-treated HeLa cell migration on fibronectin-coated μ-Slide Chemotaxis chambers following a CXCL12 gradient on top. Images over time (15 frames/s) are shown. Overlaid trajectories of cells shown in movie were detected and tracked using Fiji software.

Movie S3 (separate file)

Related to Figure 6A. Representative video of AGR1.131-treated HeLa cell migration on fibronectin-coated μ-Slide Chemotaxis chambers following a CXCL12 gradient on top. Images over time (15 frames/s) are shown. Overlaid trajectories of cells shown in movie were detected and tracked using Fiji software.

Movie S4 (separate file)

Related to Figure 6A. Representative video of AGR1.137-treated HeLa cell migration on fibronectin-coated μ-Slide Chemotaxis chambers following a CXCL12 gradient on top. Images over time (15 frames/s) are shown. Overlaid trajectories of cells shown in movie were detected and tracked using Fiji software.